Simulation of three-dimensional flow around a square cylinder at moderate Reynolds numbers

Cite as: Physics of Fluids **11**, 288 (1999); https://doi.org/10.1063/1.869879
Submitted: 22 December 1997 . Accepted: 15 October 1998 . Published Online: 06 January 1999

Ahmad Sohankar, C. Norberg, and L. Davidson

Simulation of three-dimensional flow around a square cylinder at moderate Reynolds numbers

Ahmad Sohankar
Thermo and Fluid Dynamics, Chalmers University of Technology, S-412 96 Göteborg, Sweden

C. Norberg
Division of Heat Transfer, Lund Institute of Technology, Box 118, S-221 00 Lund, Sweden

L. Davidson[a)]
Thermo and Fluid Dynamics, Chalmers University of Technology, S-412 96 Göteborg, Sweden

(Received 22 December 1997; accepted 15 October 1998)

Direct numerical simulations of two-dimensional (2D) and 3-D unsteady flow around a square cylinder for moderate Reynolds numbers (Re=150–500) are performed, employing an implicit fractional step method finite-volume code with second-order accuracy in space and time. The simulations, which are carried out with a blockage ratio of 5.6%, indicate a transition from 2-D to 3-D shedding flow between Re=150 and Re=200. Both spanwise instability modes, A and B, are present in the wake transitional process, similar to the flow around a circular cylinder. However, seemingly in contrast to a circular cylinder, the transitional flow around a square cylinder exhibits a phenomenon of distinct low-frequency force pulsations (Re=200–300). For 3-D simulations, the Strouhal number and the mean drag coefficient are in general agreement with existing experiments. Between Re=300 and 500, an increase in the spanwise coupling of fluctuating forces is indicated. The influence of the spanwise aspect ratio using periodic boundary conditions, a finer grid, and a finer time step is also investigated. © *1999 American Institute of Physics.*
[S1070-6631(99)00902-2]

I. INTRODUCTION

Over the last 100 years, the flow around slender cylindrical bluff bodies has been the subject of intense research, mainly owing to the engineering significance of structural design, flow-induced vibration, and acoustic emissions. In recent years, such studies have received a great deal of attention as a result of increasing computer capabilities, improvements in experimental measurement techniques, and increasing awareness of some new phenomena such as transitional spanwise instability modes.[1] The vast majority of these investigations has been carried out for the flow around a circular cylinder, whereas, from an engineering point of view, it is also necessary to study flow around other bluff body shapes, such as sharp-edged rectangular cross-sectional cylinders. Structures that typically have rectangular or near-rectangular cross sections include architectural features on buildings, the buildings themselves, beams, fences and occasionally stays and supports in internal and external flow geometries. The main motivation for the present study is of a practical nature. Above some critical Reynolds number, the flow around cylindrical structures exhibits the well-known time periodic phenomenon of vortex shedding. Due to the associated fluctuating forces on the body, the alternate shedding of vortices may cause structural vibrations, acoustic noise emissions (Aeolian tones), or in some cases resonance, which can trigger the failure of structures. As for the square cylinder, there is a more or less complete absence of detailed data on, e.g., mean and fluctuating forces at moderate Reynolds numbers. For instance, the only available experimental data on the mean drag coefficient for Re$\leqslant$500 can be found in the work of Okajima and co-workers.[2] There is also an academic motivation. For instance, the influence of the actual cross section in question on the transitional scenario, leading to turbulence in the wake, is of fundamental importance.[3]

It may be called for here to draw attention to some characteristics in the flow around slender cylindrical bluff bodies, as the Reynolds number is increased from about unity to approximately 500, with Re based on the cross-stream dimension, the diameter. In general terms, the following short description applies to the flow around a circular cylinder (hereafter referred to as CC flow). At low Reynolds numbers, say less than about 100, the description is also believed to be valid for the case under consideration, i.e., the flow around a square cylinder at zero incidence (hereafter referred to as SC flow). However, at higher Re, the sharp corners may play a significant role in the development of flow instabilities and other flow characteristics.

At Reynolds numbers below about unity, the flow is fully attached with no separation. As Re is increased, the flow separates, and a pair of steady symmetric vortices forms behind the body. For the circular cylinder, this occurs at around Re$\approx$3–5.[4] The recirculation region behind the body grows with increasing Re. At a critical onset Reynolds number (Re=Re_{c1}), the twin vortex arrangement becomes

a)Corresponding author. Electronic mail: lada@tfd.chalmers.se; telephone: +46 31 7721404; fax: +46 31 180976.

unstable and a time periodic oscillation of the wake develops—the Bénard–von Kármán instability.[5] The periodic phenomenon is referred to as vortex shedding, whereas the antisymmetric wake flow pattern is referred to as the von Kármán vortex street. For cylindrical structures with nonstreamlined forebodies and short afterbodies (e.g., the square cylinder), the critical Re, when scaled with the cross-stream dimension d, is $\mathrm{Re}_{c1}\sim 50$; see, e.g., Refs. 6 and 7. In Sohankar *et al.*[8] for SC flow, the reported experimental value for the onset of vortex shedding is $\mathrm{Re}_{c1}=47\pm 2$ (solid blockage, $\beta=0.25\%$) whereas in previous numerical investigations, e.g., for $\beta=5.0\%$ in Ref. 9 and $\beta=14.2\%$ in Ref. 10, the reported onset values are $\mathrm{Re}_{c1}=51.2$ and 53, respectively. Presumably, the critical onset Re value increases with increasing blockage. By increasing the Reynolds number in CC flow, a hysteretic (subcritical) 3-D transition at $\mathrm{Re}=\mathrm{Re}_{c2}\approx 170-190$ develops.[1,11]

Within the laminar shedding régime, which is between these two instabilities ($\mathrm{Re}_{c1}<\mathrm{Re}<\mathrm{Re}_{c2}$), the vortex shedding is characterized by a fundamental shedding frequency (f_S) of extremely high spectral quality, which, when nondimensionalized with the viscous time scale d^2/ν, for both CC and SC flow, exhibits an approximate linear increase with the Reynolds number.[9,12] On the basis of experiments reported in Ref. 9, the vortex shedding frequency in laminar shedding SC flow varies according to

$$\frac{f_S d^2}{\nu}=\mathrm{St}\times\mathrm{Re}\simeq -3.7+0.18\times\mathrm{Re}, \tag{1}$$

where St is the Strouhal number. Previous numerical work by the authors[8,13] for SC flow at $\beta=5\%$ shows that the separation for $\mathrm{Re}\leqslant 100$, at all times in the fully saturated state, occurs from the rear corners, predominantly from the rear corners at $\mathrm{Re}=125$ with occasional upstream corner separation, predominantly from upstream corners at $\mathrm{Re}=150$, and, finally, at all times, from upstream corners for $\mathrm{Re}\geqslant 175$. This is in reasonable agreement with Franke *et al.*,[14] who, at $\beta=8.3\%$, report separation from upstream corners for $\mathrm{Re}>150$.

The second wake instability, occurring at around $\mathrm{Re}=\mathrm{Re}_{c2}$, has been extensively studied in CC flow—experimentally, numerically, and theoretically, see, e.g., Refs. 1, 3, 11, 15–19. By contrast, at least to the knowledge of the present authors, there are as yet no such published studies in SC flow, although some theoretical work in this direction is known to be in progress at the University of Illinois at Urbana—Champaign (S. Balachandar and coworkers). However, as this wake transition has been suggested to be the result of an elliptic instability of the vortex cores in the near wake,[1] it may be conjectured that a similar transitional behavior also occurs in SC flow.

In CC flow, the (3-D) wake transition regime is reported to be approximately between Re_{c2} and $\mathrm{Re}=260$; see Ref. 19. Today, it is well known that this regime, in CC flow, involves two modes of spanwise instabilities (modes A and B).[1,15] The long-wavelength mode A instability develops at $\mathrm{Re}=\mathrm{Re}_{c2}$ and at onset has a spanwise wavelength of about four diameters; see Barkley and Henderson (1996).[11] The short-wavelength mode B instability, appearing at around $\mathrm{Re}\approx 230$, has a wavelength of the order of one diameter, which scales with the braid shear layer between the primary (von Kármán) vortices.[1]

The motivation for the present study is the obvious lack of information concerning transitional features in SC flow. Is the transitional scenario in SC flow similar to CC flow? Some preliminary experiments carried out by the second author here indicate that, in low blockage SC flow the 2-D/3-D transition has some similarities with CC flow and occurs at around $\mathrm{Re}=150$; see Ref. 8. Further, in CC flow, there is a peak in base suction at around $\mathrm{Re}=260$ (at the end of the so-called wake transitional regime), where the shedding frequency retrieves its extremely narrow band character from the laminar shedding regime.[15,20] Does this also happen in SC flow?

The objective of this work is to investigate the inherent three-dimensional features present in transitional SC flow, to make comparisons with 2-D results, and to present reliable data on global quantities for moderate Reynolds numbers ($\mathrm{Re}=150$–500).

II. NUMERICAL METHOD

A. Physical and mathematical formulation

The flow is described in a Cartesian coordinate system (x,y,z) in which the x axis is aligned with the inlet flow direction (streamwise direction), the z axis is parallel with the cylinder axis (spanwise direction), and the y axis is perpendicular to both these directions (cross-stream direction). The origin is centered on the downstream face of the cylinder; see Fig. 1. The fixed two-dimensional square cylinder with a side d is exposed to a constant free-stream velocity, U_∞. Incompressible flow with constant fluid properties is assumed. The Reynolds number is defined as $\mathrm{Re}=\rho U_\infty d/\mu$ (ρ is the density and μ is the dynamic viscosity of the fluid). All geometrical lengths are normalized with d, velocities with U_∞, physical times with d/U_∞, and frequencies with U_∞/d. Consequently, the Strouhal number is defined as $\mathrm{St}=f_S d/U_\infty$, where f_S is the shedding frequency. Force and pressure coefficients are normalized with the dynamic pressure, $\rho U_\infty^2/2$. In the y direction, the vertical distance between the upper and lower walls, H, defines the solid blockage of the confined flow (blockage parameter, $\beta=1/H$).

By using standard notation for Cartesian tensors, the governing equations for the flow under consideration can be written as

$$U_{i,i}=0, \tag{2}$$

$$\frac{\partial U_i}{\partial t}+(U_i U_j)_{,j}=-P_{,i}+\mathrm{Re}^{-1}\,U_{i,jj}, \tag{3}$$

where indices $i=1,2,3$ refer to the streamwise (x), crosswise (y), and spanwise (z) directions, respectively.

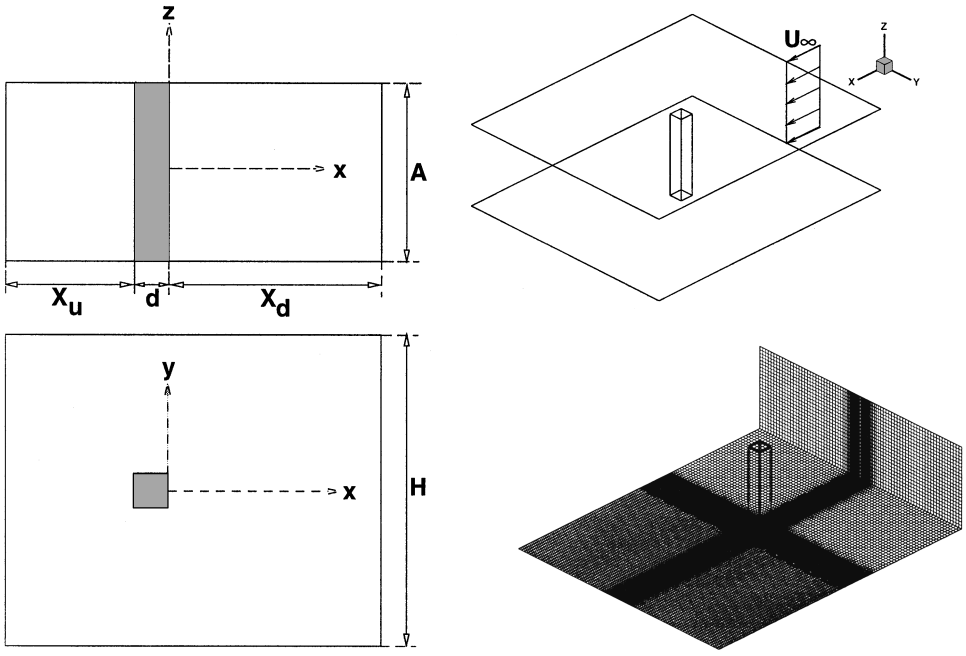

FIG. 1. Flow configuration and standard grid in xy and yz planes.

B. Time step, calculation domain, and boundary condition

The time marching calculations were started with the fluid at rest. Except for case 16 in Table I for Re=500, a constant time step $\Delta t=\frac{1}{40}=0.025$ was used for all simulations. For case 16, Δt was 0.0125.

The grid distribution was made uniform with a constant cell size, Δ, outside a region from the body that extended two units upstream, downstream, and sideways (in the x and y directions). Downstream of the body, Δ was set to 0.15, except for the fine grid at Re=500, where $\Delta=0.1$ prevailed. In other parts, $\Delta=0.25$ was used. The distance from the cylinder surface to the nearest grid point defines δ. For this study, $\delta\approx 0.004$ on the upstream surface, 0.006 on side surfaces, and 0.008 on the downstream surface. The hyperbolic tangent function was used for stretching the cell sizes between these limits (δ and Δ); see Fig. 1. In the spanwise direction (the z direction, with length A), a uniform grid with a distance of Δ_z between nodes was used. In this study, $\Delta_z=0.25$, except for the fine grid at Re=500, where $\Delta_z=0.15$. The number of nodes distributed over one unit length of the cylinder surface was set equal to 25 for all sides of the body, except for the fine grid at Re=500, where the number of surface nodes was increased to 33 on the vertical (front and back) sides of the body.

At the inlet, which is located X_u units upstream of the cylinder, a uniform flow was prescribed ($U_1=1, U_2=U_3=0$). At the outlet, which is located X_d units downstream of the body, the convective boundary condition $[\partial U_i/\partial t+U_c(\partial U_i/\partial x)=0]$ was used for all velocity components.

TABLE I. Summary of results. A is the spanwise aspect ratio of the cylinder (not applicable for 2-D). Here γ_D and γ_L are the ratios between spanwise-averaged to spanwise-mean sectional rms drag and lift, respectively (D' and L' are spanwise-averaged rms values of drag and lift). Cases 1–15: $\Delta t=0.025$; case 16: $\Delta t=0.0125$.

Case		Re	Grid	A	St	C_D	D'/L'	$C_{L'}$	γ_D	γ_L
1	2-D	150	169×121	⋯	0.165	1.44	0.044	0.23	⋯	⋯
2	3-D	150	169×121×25	6	0.165	1.44	0.044	0.23	1.00	1.00
3	2-D	200	169×121	⋯	0.170	1.46	0.069	0.32	⋯	⋯
4	3-D	200	169×121×25	6	0.157	1.39	0.155	0.21	0.76	0.98
5	3-D	200	169×121×41	10	0.160	1.41	0.105	0.22	0.69	0.93
6	2-D	250	169×121	⋯	0.154	1.49	0.068	0.52	⋯	⋯
7	3-D	250	169×121×25	6	0.159	1.43	0.152	0.21	0.64	0.98
8	3-D	250	169×121×41	10	0.158	1.43	0.092	0.20	0.46	0.93
9	2-D	300	169×121	⋯	0.138	1.56	0.118	0.81	⋯	⋯
10	3-D	300	169×121×25	6	0.153	1.47	0.116	0.20	0.49	0.98
11	2-D	400	169×121	⋯	0.145	1.67	0.234	0.94	⋯	⋯
12	3-D	400	169×121×25	6	0.136	1.67	0.055	0.64	0.44	0.99
13	2-D	500	169×121	⋯	0.174	1.89	0.318	1.13	⋯	⋯
14	3-D	500	169×121×25	6	0.126	1.87	0.114	1.23	⋯	⋯
15	3-D	500	209×129×41	6	0.127	1.84	0.097	1.14	0.85	0.999
16	3-D	500	209×129×41	6	0.122	1.84	0.123	1.22	0.87	0.998

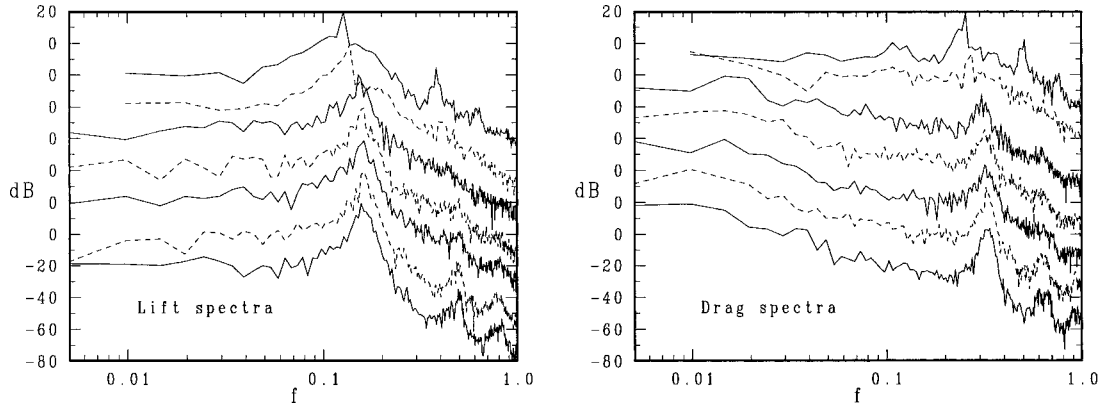

FIG. 2. Lift and drag spectra from 3-D simulations. Left: from fluctuating lift. Right: from fluctuating drag. Bottom to top: (Re,A)=(200,6), (200,10), (250,6), (250,10), (300,6), (400,6), (500,6); case 15. Here $n_d=2$. Ordinate: $dB=10\log G$, where G the one-sided autospectral density function scaled with the variance of the signal. Please note the 20 dB shift between successive cases.

As in Ref. 9 the value of U_c was set equal to unity. No-slip conditions were prescribed at the body surfaces. At the upper and lower boundaries symmetry conditions simulating a frictionless wall were used ($U_{1,2}=U_{3,2}=U_2=0$). A periodic boundary condition was used in the spanwise direction for 3-D simulations. The spanwise dimension A (Fig. 1) was set equal to $A=6$ and $A=10$; see Table I. The normal derivative for the pressure was set to zero at all boundaries. Dimensions X_u, X_d, and H were set to 8.5, 12.5, and 18, respectively; see Fig. 1.

C. Numerical solution

An incompressible finite volume code with a nonstaggered grid arrangement was used. After discretization, Eqs. (2) and (3) were solved with an implicit fractional step method. All terms in the momentum equation (3) were advanced in time using the modified Crank–Nicolson scheme,[21] as follows:

$$U_i^{n+1}=U_i^n+\Delta t H(U_i^n,U_i^{n+1}) - \alpha\Delta t P_{,i}^{n+1}-(1-\alpha)\Delta t P_{,i}^n, \tag{4}$$

where superscripts n and $n+1$ denote old and new time levels, respectively, and $H(U_i^n,U_i^{n+1})$ includes convection and diffusion terms, i.e.,

$$H(U_i^n,U_i^{n+1})=\alpha\ \mathrm{Re}^{-1}\ U_{i,jj}^{n+1}+(1-\alpha)\mathrm{Re}^{-1}\ U_{i,jj}^n - \alpha(U_i^{n+1}U_j^{n+1})_{,j} - (1-\alpha)(U_i^nU_j^{n+1})_{,j}. \tag{5}$$

In the present study α was set to 0.6.

The numerical solution procedure for obtaining U_i and P at each time step can be summarized as follows.

(1) Solve the discretized equations (4) for obtaining U_i^{n+1} by rearranging to a standard form of control volume formulation. For example, the standard form of the U equation ($i=1$) is

$$a_PU_P^{n+1}=\sum\ a_{nb}U_{nb}^{n+1}+b, \tag{6}$$

where

$$b=(1-\alpha)\sum\ a_{nb}U_{nb}^n+\left(a_P^0-(1-\alpha)\sum\ a_{nb}\right)U_P^n+S,$$

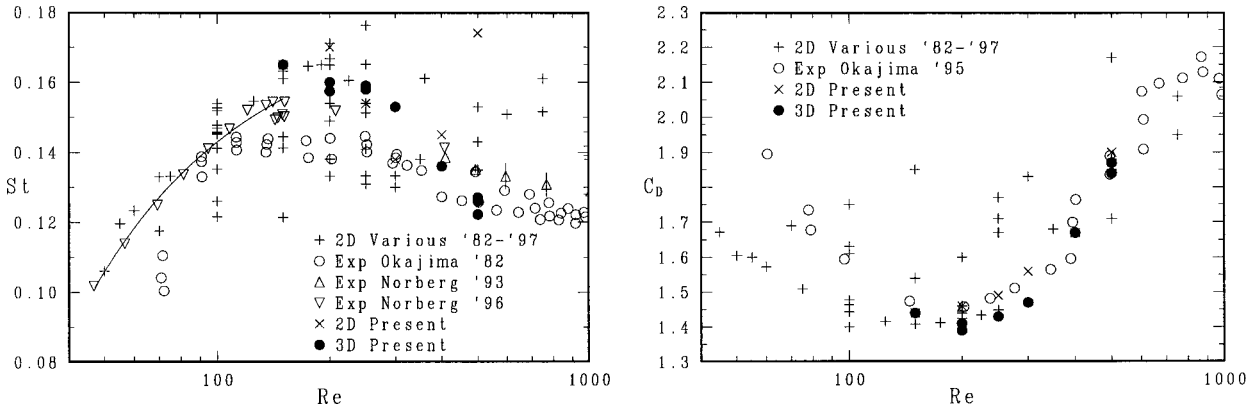

FIG. 3. Strouhal number (left) and mean drag coefficient (right) versus Re. The solid line corresponds to St=0.18−3.7/Re, as suggested from the laminar shedding data of Norberg 1996.

$a_P^0=(\Delta t)^{-1}\delta V$ (δV is the cell volume),

$$a_P=a_P^0+\alpha\sum a_{nb}.$$

The gradients of pressure in Eq. (4) (levels n and $n+1$) are put in the source term (S). At this stage, the most recent values of pressure and velocities are used to obtain U_i^{n+1}.

(2) Intermediate velocities are defined as

$$U_i^*=U_i^n+\Delta tH(U_i^n,U_i^{n+1})-(1-\alpha)\Delta tP_{,i}^n. \tag{7}$$

By using Eq. (4), U_i^* can be calculated as

$$U_i^*=U_i^{n+1}+\alpha\Delta tP_{,i}^{n+1}. \tag{8}$$

The intermediate velocity field (U_i^*) does not satisfy the continuity equation. Velocities at control volume faces (U_{face}^*) are calculated by interpolating from neighboring intermediate velocities at nodes. These interpolated cell face velocities are used to calculate the mass fluxes and convection terms.

(3) To satisfy continuity for $U_{i(\text{face})}^{n+1}$, take the divergence of Eq. (8) and insert $U_{i(\text{face}),i}^{n+1}=0$, thus

$$P_{,ii}^{n+1}=(\alpha\Delta t)^{-1}U_{i(\text{face}),i}^*. \tag{9}$$

This is the Poisson equation for obtaining pressure on level $(n+1)$. This equation is solved with a multigrid Poisson solver.[22]

(4) The cell face velocities are corrected. For example, the U component ($i=1$) is written as

$$U_{\text{face}}^{n+1}=U_{\text{face}}^*-\alpha\Delta t\left(\frac{\partial P^{n+1}}{\partial x}\right)\Bigg|_{\text{face}}. \tag{10}$$

These velocities are used to calculate the mass fluxes at faces of control volume that are used to satisfy the continuity equation.

Stages (1)–(4) are carried out for each iteration until a global convergence criteria for continuity and momentum equations at each time step is fulfilled.

D. Evaluation of the data

1. Stationary flow condition

Constancy within ±1% in the calculated rms values of fluctuating lift and drag, as deduced by employing different initial integration times, was used as a criterion for flow stationarity. The transient period before this stationary condition was achieved varied from case to case, e.g., the transient period for case 4 in Table I (Re=200, $A=6$) was about 240 time units whereas case 14 (Re=500, $A=6$) needed only about 50 units to reach this fully developed state (extreme cases). For all cases, the time spent in the saturated condition was greater than 25 shedding periods. However, the flow for the 3-D cases at Re=200 and Re=250 exhibited a seemingly random pulsation with time, roughly with a repetition period of 60–100 time units (10–16 shedding periods); see Figs. 4 and 7. For these cases, the saturated time required to establish valid statistical quantities was extended to be at least 50 shedding periods, corresponding to about 320 time units.

2. Strouhal number

The present Strouhal numbers (Table I) were determined from the fluctuating lift signals in the stationary flow condition. For each case, the actual dominating peak frequency in the calculated power spectral density (PSD) was determined as the mean value between the two frequencies that were 3 dB down from the peak value. The spectral analysis was based on the standard Cooley–Tukey FFT algorithm, where the number of values in each of the n_d data segments was set equal to $N=2^p$ (p is an integer). To reduce sidelobe effects in the spectral evaluation, a cosine taper over 10% of each end of the data segment was applied; see Ref. 23. The spectral linewidth of the analysis is f_d/N, where $f_d=(\Delta t)^{-1}$ is the data frequency. To avoid aliasing, the signals were low-pass filtered with a cut frequency equal to 0.45 times the data frequency. The Strouhal numbers were based on evaluations using a spectral linewidth of about 0.005 units, corresponding to a resolution of about 3.5% (in terms of the Strouhal number).

3. Spanwise correlation of lift and drag

Assuming flow homogeneity in the spanwise direction, the following simple formula for the ratio, γ, between a rms force component on a finite segment l of the cylinder and the rms sectional force ($l\to 0$) can be derived (see, e.g., Kacker *et al.*[24]):

$$\gamma=l^{-1}\sqrt{2\int_0^l(l-s)R(s)ds}, \tag{11}$$

where $R(s)$ is the correlation coefficient between sectional forces separated a spanwise distance s apart. The one-sided spanwise correlation length is defined as

$$\Lambda=\int_0^\infty R(s)ds. \tag{12}$$

In laboratory experiments, the upper bound should be chosen to be much larger than the actual spanwise correlation length (the integral is assumed to be convergent). In flows with a limited spanwise correlation, the exponential decay, $\exp(-s/\Lambda)$, can be used as an approximation for the correlation function, R. The ratio then becomes

$$\gamma=\frac{\sqrt{2}}{a}[\exp(-a)+a-1]^{0.5}, \tag{13}$$

where $a=l/\Lambda$. Is this analysis really applicable to the present simulated data? If so, when using $l=A$, the correlation length of sectional lift and drag forces can be estimated from the ratios γ_L and γ_D, respectively. The criterion of spanwise homogeneity was fulfilled—at least for the time-averaged mean lift and drag for which the spanwise variations in C_L and C_D were within ±0.005 and ±1%, respectively. However, the variations in the (time-averaged) sectional rms lift and drag were significantly higher with standard deviations in the order of 2% and 15%, respectively. When the integration time was increased, these variations diminished. Except for small separation distances (s

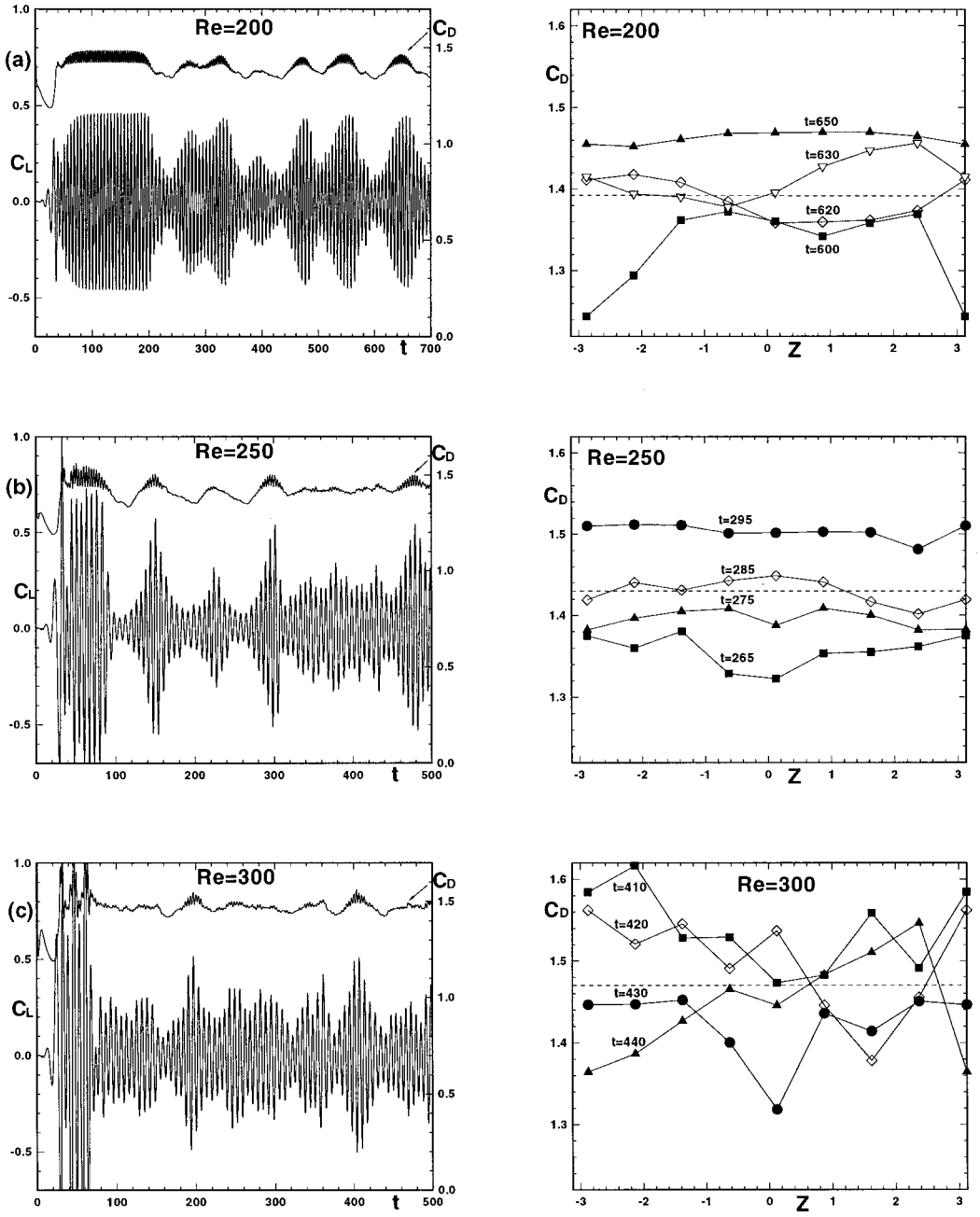

FIG. 4. Spanwise-averaged lift and drag coefficient versus time (left) and instantaneous sectional drag coefficient at different times and spanwise locations (right). Here $A=6$. (a) Re=200, (b) Re=250, (c) Re=300.

<0.8, approximately), the exponential drop in the spanwise correlation coefficient seemed to be a reasonable approximation of the simulated data.

III. VALIDATION

A summary of global results in the stationary condition is compiled in Table I.

For a direct numerical simulation (DNS), the spatial and time resolution (time step) should be sufficiently fine to resolve all scales of the fluid motion. Other numerical factors, such as convergence criterion, arithmetic precision, and the positions of upstream and downstream domain boundaries must be considered. It is also necessary for physical validation to investigate the influence of the computational spanwise distance (A). If this distance is chosen to be too small, important instability modes and/or dynamically important interactions between such modes can be inhibited.[3] Although not really applicable, the 2-D simulations can be regarded as having $A=0$. If possible, the data should also be critically compared with the results of previous investigations.

A. Influence of numerical parameters

In previous works of the authors[8,9,13] for $\mathrm{Re}\leqslant 200$ and 2-D flow, an extensive study was made of various computation parameters such as the size of the computation domain,

time step, near- and farfield resolution, distribution of grid nodes on the side of the body, and the effect of the outlet boundary condition. In general, see Table I, a (169×121) grid was used in the xy plane, which is finer than the most refined grids used in earlier studies of this group. At Re =500, which is the highest Re, a 1.1 million point grid (209 ×129×41) with two time steps (cases 15 and 16 in Table I) was used to ensure validity. For these cases, as compared with the standard grid, the spatial refinement in the spanwise direction was 40%, whereas the refined time step was half the standard value. As is evident from Table I, the rms drag was more sensitive than other quantities to variations in the computational spanwise length and spatial/time resolution. The fluctuations in drag were shown to be closely related to the actions of secondary wake structures, which, in turn, have significant dynamic ingredients of streamwise vorticity; e.g., see Figs. 14 and 15. Moreover, at higher Re, approximately Re>250, the flow also involves the formation of small-scale vortical structures; e.g., see Fig. 11(b). In the sensitivity study at Re=500, the maximum changes in St, C_D, $C_{D'}$, and $C_{L'}$ were about 3%, 1.6%, 20%, and 7%, respectively. It is interesting to note that the effect of a finer grid (case 15) and a finer grid with a finer time step (case 16) work in a way opposite to that of the standard case (case 14); see Table I. If the standard case (case 14) is compared with case 16, which may be more correct, owing to Courant number considerations, the above mentioned differences between global results are reduced to a maximum of 7%.

During the iterative sequence, convergence was assessed at the end of each iteration on the basis of the residual sources criterion, which compares the sum of the absolute residual source over all the control volumes in the computation field, for each finite volume equation and pressure. The residuals for the continuity and momentum were normalized with the incoming mass flux and momentum flux, respectively. The convergence criterion was set to 0.001, i.e., the normalized residual for the U_i equation and the continuity equation was smaller than 0.001. Tests with a convergence criterion of 0.0001 and double precision showed no significant changes in the results (e.g., less than 0.8% for the rms lift), whereas the number of iterations for convergence increased by approximately a factor of 2.

Thus, at least for the nonuniform grids employed in this investigation and for such moderate Reynolds number vortex shedding flows, it is suggested that the simulations were close to being direct numerical simulations.

B. Influence of aspect ratio (including comparison 2-D/3-D)

The influence of increasing the spanwise length, A (the aspect ratio), from zero (2-D simulations) to $A=6$ (3-D simulations) was investigated for all Reynolds numbers; see Table I. Despite all other very significant and dramatic effects (see below) noted by introducing this spanwise dimension, there was a rather small influence on the mean drag coefficient, C_D, the maximum decrease being about 6% (Re =300). The 3-D simulation at Re=150 did not exhibit any spanwise variations and thus produced the same global quantities as for the 2-D simulation. For Re≥200 the associated effects on the Strouhal number St were complex; a rather small decrease was noted for Re=250 (−3%), whereas moderate to significant changes were noted at other Re (−27% to +10%). The most dramatic effects occurred for the fluctuating forces. At Re=300 and for rms lift, there was a reduction by a factor of 4 when comparing $A=6$ with the corresponding 2D simulation (cases 9 and 10 in Table I). For Re=200, 250 the 3-D simulations produced significantly higher sectional rms drag coefficients ($=C_{D'}/\gamma_D$) while the opposite was true for higher Re. For these two Re and with a subsequent increase in the spanwise dimension from $A=6$ to $A=10$, there was instead a decrease in the sectional rms drag with small to negligible effects on St, C_D, and rms lift.

When comparing spanwise-averaged 3-D results (cases 14–16) with 2-D results (case 13) at Re=500 for C_D, $C_{D'}$, $C_{L'}$, and Strouhal number, St, the differences were about −3%, −63%, +6%, and −27%, respectively. However, for 3-D simulations at this Re, owing to the apparently very high spanwise correlation of sectional lift fluctuations (Sec. V B), the mean drag and rms lift were probably overpredicted and the Strouhal number underpredicted. The large discrepancy for the rms drag can be directly attributed to three-dimensional effects, which, of course, are inhibited in 2-D simulations. The frictional mean drag coefficients were very small, the values for Re=500 being about −0.04 and −0.05 in 2-D and 3-D simulations, respectively. For Re=500 (case 15), some mean and rms pressure coefficients at positions around the cylinder surface were also calculated. For example, the mean and rms base pressure coefficients (C_{Pb}, C'_{Pb}) were (−1.26, 0.48) for the 2-D simulation and (−1.24, 0.29) for the 3-D simulation. The difference in C_{Pb} is less than 2%, whereas the difference for C'_{Pb} is about 40%. The C_P values at the low-pressure point ($C_{p,\min}$) on the wake centerline for the 2-D and 3-D simulations were significantly different (2-D: −2.04, 3-D: −1.64). In the 2-D simulation, this point also occurred closer to the body than in the 3-D simulation; see Fig. 17(b). Similar changes when comparing 2-D and 3-D simulations have been reported by Mittal and Balachandar[25] for circular and elliptic cylinders (Re=525).

C. Comparison with previous data

Figure 3 gives a comparison between the present 2-D and 3-D simulations, together with the experimental results of Okajima,[2] Norberg,[8,26] and others (2-D numerical) for the Strouhal number St and mean drag coefficient C_D. The present 3-D results were in general agreement with the experiments.

The mean drag coefficients of the present study are in reasonable agreement with the experimental results of Okajima.[2] As for the Strouhal number, the differences compared with experiments appear to be higher, especially at around Re=150–300, which is presumably within the transition region from 2-D to 3-D flow (Sec. V C). The present investigation, which is purely numerical and carried out at a blockage ratio of 5.6%, indicated that the transition from 2-D to 3-D flow occurs within the interval of Re=150 to Re=200 while low blockage ($\beta=0.25\%$) experiments of Norberg (in

Ref. 8; see Fig. 3) indicate that the transition occurs at around Re=150. Most other 2-D numerical results have higher blockages, e.g., $\beta \simeq 8\%$ ($H=12-13$) in Refs. 14, 27–30. For Re$\leqslant$200 in Fig. 3, the experiments of Okajima *et al.*[2,31] are carried out at $\beta \leqslant 3.6\%$. The estimated uncertainty of this data is on the order of 5% (Okajima[32]). The local acceleration effects caused by blockage presumably stabilize the flow, thus producing higher transitional Reynolds numbers. Moreover, in 2-D shedding flow, as shown in, e.g., Refs. 9, 13, and 33, the effect of an increase in β is to produce higher values of St and C_D. Thus, when comparing the present results with available experimental data, it is suggested that the blockage effect can explain both the apparent disagreement in 2-D flow Strouhal number at around Re=150 and the apparent discrepancy in the critical Re for the transition from 2-D to 3-D flow. When considering the blockage effect and experimental uncertainties, the Strouhal numbers for Re$\leqslant$400 were in general agreement with experiments.

As regards the Strouhal number at Re=500, however, it seems that the difference between the experimental value of Norberg[26] (St=0.135) and the present 3-D results cannot be explained simply by referring to the blockage effect and/or experimental uncertainties. The present data (cases 14–16 in Table I) are about 6%–10% lower than the data of Norberg[26] for which a conservative estimate of the experimental uncertainty is $\pm 1.5\%$ (1% blockage, endplates, aspect ratio 120). At these Re, at least to the first order, the local acceleration caused by blockage will probably also speed up the shedding process, producing a higher Strouhal number. However, as the blockage will then act as an effective increase in Re, the slight downward trend of St versus Re in this range might diminish the anticipated increase in the Strouhal number, owing to blockage. The spatial and subsequent time refinement (cases 15 and 16) caused only minor changes in the Strouhal number (variations within $\pm 2\%$) as compared with the standard grid and time step case. It is suggested that the apparent discrepancies for Re=500 are related to the computational spanwise length of the cylinder, the aspect ratio A. For Re=500 and $A=6$, as evidenced by the near-unity ratios γ_D and γ_L (Table I), the spanwise coupling of forces was extremely high. A larger aspect ratio will presumably decrease the level of sectional forces. The recent simulations by Henderson[3] for CC flow at Re=1000 show that there is a decrease in the level of sectional drag with an increase in the aspect ratio (from $A=6.3$ to $A=25$). The effect of the computational aspect ratio for SC flow is unknown. However, the trend of the SC data (Fig. 3) suggests that a decrease in the level of forces will produce an increase in the Strouhal number. Nevertheless, for Re$\geqslant$300, owing to limitations in the available computational resources, the suggested influence of the aspect ratio was not pursued in this study. Global data on rms lift and drag are also compiled in Table I. To the authors' knowledge, there are no 3-D numerical or experimental results with which comparisons can be made.

When considering experimental uncertainties, different experimental conditions, especially end conditions, blockage and effects caused by various numerical parameters including the computational aspect ratio, the agreement with previous results seems satisfactory.

IV. 2-D SIMULATIONS

The lift and drag spectra from 2-D simulations exhibited a scenario of period doubling (spectra not shown; signals for Re=400, 500 shown in Fig. 5). Up to Re=250, there was no sign of any period doubling in the calculated spectra, i.e., there were no peaks below the fundamental at $f=f_1$. However, for Re$\geqslant$300, the spectra exhibited an increasing number of additional peaks, among them peaks at $f=\frac{1}{2}f_1$ and $f=\frac{3}{2}f_1$. The peak spectral value at $\frac{1}{2}f_1$ for both C_D and C_L actually became dominant for Re=500, the highest peak in the spectra being at $f \simeq 0.087$, which is half the value reported in Table I (case 13, St=0.174). For Re=500, a peak at $\frac{1}{4}f_1$ was also discernible in the spectrum of lift fluctuations. This additional period doubling can be inferred directly from the lift signal in Fig. 5(b). It should be mentioned that for Re$\geqslant$300, approximately, in the stationary condition, the time–mean flow patterns were not perfectly symmetric with respect to the oncoming flow. For instance, the time–mean lift coefficient for Re=400 was equal to $C_L=-0.04$. The vorticity field at the instant of minimum lift for Re=500 is shown in Fig. 6. At $x \approx 8$, two oppositely signed von Kármán vortices are grouped as a pair that convects away from the wake centerline. The wake pattern has some similarity to the vortex street behind a cylinder vibrating transversely at high amplitudes and frequencies below the fundamental shedding frequency.[34] As results from 2-D simulations were not of primary concern in the present study, this apparent similarity and other flow characteristics were not pursued further. For comparison with the 3-D simulated near-wake spanwise vorticity field at minimum lift for Re=500, see Fig. 16(b).

Period doubling is one possible path or scenario of transition to turbulence in fluid systems.[35] In CC flow, a cascade of period doublings without merging of spanwise (von Kármán) vortices has been observed for Re$\geqslant$300[35,36] ($A=1.6,3.1$). Vortex merging was also absent in the present simulations. Henderson[3] recently reported that a period doubling scenario seems reasonable when the complexity of the large system is eliminated by using a spanwise length smaller than the lowest 3-D unstable spanwise wavelength. This is in accordance with the results of Thompson *et al.*,[37] who, in CC flow for Re=250, report period doublings in simulations using $A=1.6$ but not for larger spanwise domains ($A=3.1,6.3$). Obviously, in 2-D simulations of inherently 3-D, flow, i.e., for Reynolds numbers above the critical onset value for mode A instabilities, the structure of flow in the spanwise direction is completely eliminated. It seems that the existence of period doublings for Re$\geqslant$300 in the present 2-D simulations is in agreement with Henderson's[3] suggestion.

V. 3-D SIMULATIONS

A. Lift and drag spectra

Figure 2 depicts some lift and drag spectra from 3-D simulations in the stationary flow condition (Re=200 to Re

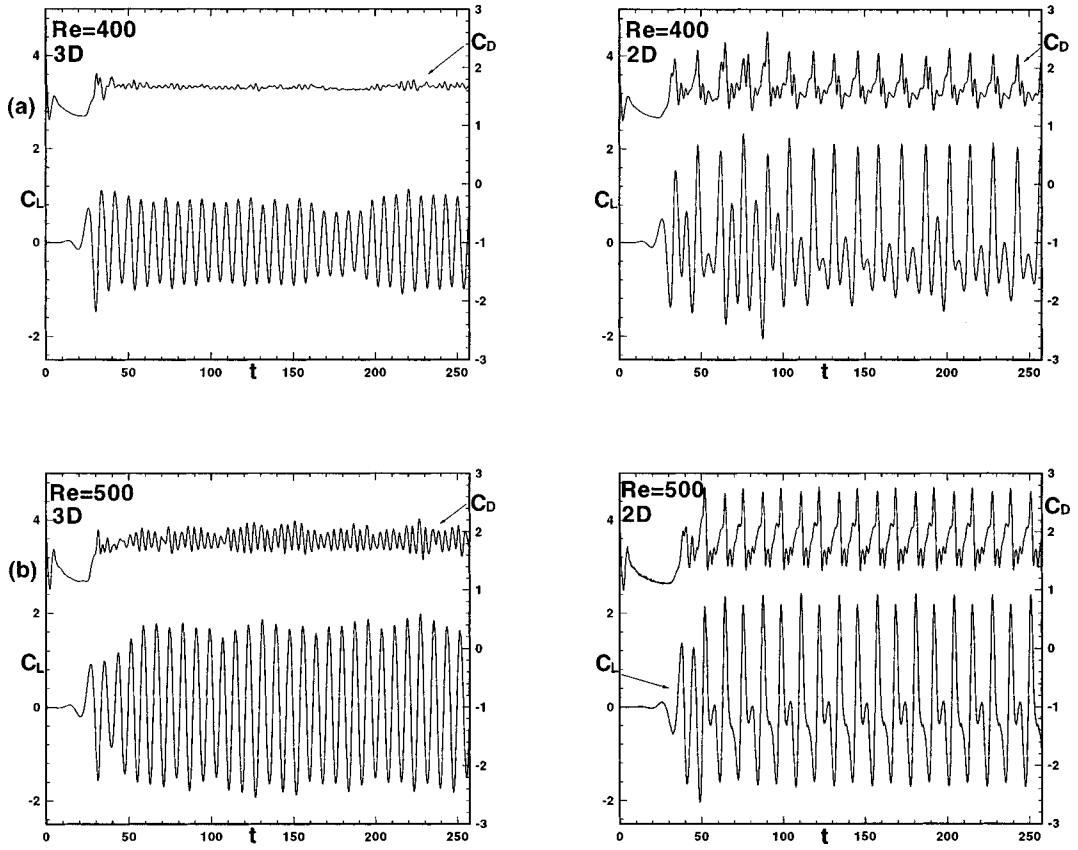

FIG. 5. Lift and drag coefficients versus time. Left: 3-D simulations, $A=6$, spanwise-averaged. Right: 2-D simulations. (a) Re=400, (b) Re=500.

=500, $n_d=2$). Individual spectra at a finer resolution and the resulting although less frequency resolved spectra based on more than two data segments (e.g., $n_d=4$) did not show any significant changes in the general appearance. For all 3-D cases, the fluctuating lift was completely dominated by fluctuation energy at around the time mean shedding frequency, i.e., the Strouhal number. Odd harmonics of the shedding frequency (3×St, 5×St, ...) also appeared in the lift spectra, especially for Re=200 and Re=500; see Fig. 2 (left). However, the fluctuation energy associated with these secondary peaks was extremely small. Owing to the limited spectral resolution and statistical accuracy, it was not possible to determine whether the spectra exhibited a twin peak behavior, as is present in a transitional CC flow.[19] The drag spectra exhibited peaks at even harmonics of the shedding frequency (2×St, 4×St, ...). A substantial part of the drag fluctuation energy was concentrated to frequencies of the order 0.01, however, and especially so for Re=200 and Re =250; see Fig. 2 (right).

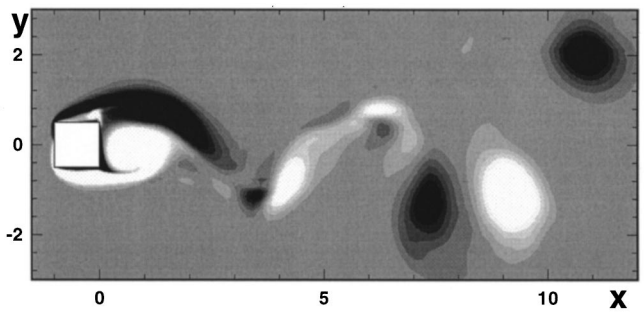

FIG. 6. Instantaneous vorticity field (ω_z) for Re=500 from the two-dimensional simulation (case 13, $\Delta\omega_z=0.4$). Instant of minimum lift ($t=177.6$, $C_D=2.0$, $C_L=-2.2$).

B. rms lift and drag, spanwise correlations

The relation between the spanwise-averaged rms lift and drag and the corresponding sectional forces are described by the ratios γ_L and γ_D, respectively (Table I). For Re≥200, the 3-D-simulated sectional rms lift was four to nine times higher than the sectional rms drag, as compared with the laminar shedding case Re=150, for which the corresponding ratio was 23. Associated with the transition to three-dimensional flow (between Re=150 and Re=200), there was an increase in rms drag and a decrease in rms lift.

The choice of aspect ratios in the present study was guided from the recent findings on three-dimensional instability modes, as found in circular cylinder wakes (CC flow).[3,11] In CC flow, see, e.g., Ref. 3, the upper spanwise limit of the unstable (mode A) wave number band increases from about 4 diameters at onset to a level of about 6.7 diameters at higher Re (Re>300). The basis of the present study was that the corresponding diagram for SC flow is similar to CC flow, at least with regard to its upper limit. Some indications of the Reynolds number dependence on the spanwise coupling of forces were found from the correlation analysis, as outlined in Sec. II D 3. On drag forces, the indicated cor-

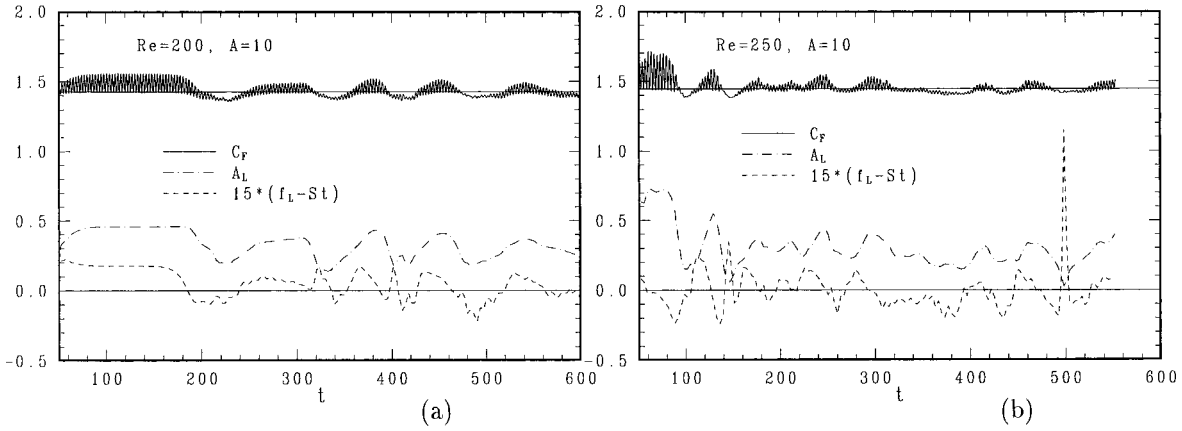

FIG. 7. Time evolution of spanwise-averaged force coefficient $C_F=\sqrt{C_D^2+C_L^2}$, lift envelope amplitude coefficient, A_L, and lift shedding frequency, f_L, for aspect ratio $A=10$. (a) Re=200, (b) Re=250. Offsets for f_L are the Strouhal numbers from Table I (in both cases, the mean shedding period in the stationary condition is about 6.3 time units).

relation lengths at Re=200, 250, 300, 400, and 500 were about 3.3, 1.5, 0.8, 0.7, and 6 diameters, respectively (lift and drag signals at different spanwise positions were not saved for case 14, i.e., for Re=500, using standard parameters, hence the missing values in Table I). The indicated correlation lengths associated with drag, for Re$\leqslant$400, were of the same magnitude as the spanwise extent of these structures, which gives some creditability to the analysis. On lift forces, the indicated spanwise correlation lengths were significantly higher. For Re=200, 250 and $A=10$, the indicated correlation length was about 22 diameters. Surprisingly, for Re $>$250, the indicated spanwise coupling of lift forces increased with increasing Re. At such high lift ratios ($\gamma_L \geqslant 0.98$), the indicated correlation lengths are extremely sensitive to the actual level of the ratio ($\gamma_L > 0.98$; $A=6$ implies a correlation length greater than about 50 diameters). An extremely high correlation of lift forces was indicated for Re=500. However, a correlation length much longer than the actual aspect ratio is actually an indication that a longer computational aspect ratio might be needed for physical realization. Due to limited computational resources and the extremely long simulation times involved, it was not possible to investigate the effects of aspect ratio at all simulated Reynolds numbers. Nevertheless, for Re=500, the seemingly good prediction of rms lift from a 2-D simulation (case 13 in Table I) is believed to be an effect of this indicated strong spanwise coupling of lift forces. For all other cases at Re$\geqslant$200, the rms lift from 2-D simulations were significantly higher than those in 3-D simulations.

C. Transitional Reynolds number

Experiments by the second author[8] indicated that the transition from 2-D to 3-D flow occurs at around Re=150. At higher Re, the shedding frequency became broadbanded and therefore difficult to trace with the period counter that was used on this occasion. These low blockage experiments were carried out with an aspect ratio of 200 using circular cylinders at the ends to promote the parallel shedding condition in the laminar shedding regime (the end cylinder diameter was three times the side dimension of the square cylinder). However, the degree of parallelity was not investigated. Nevertheless, within the experimental uncertainty, which was estimated to be $\pm 2.5\%$ for both Re and St, there was no sign of any previous jump in the St–Re relationship between the onset of vortex shedding and the small jump associated with the region of double-valued Strouhal numbers in between approximately Re=140 and Re=150; see Fig. 3(a).

It was not possible from the present data to obtain the exact, presumably hysteretic,[11] critical Reynolds number range for which the transition from 2-D to 3-D flow occurs in an unbounded domain (no blockage). However, the present simulations at a blockage ratio of 5.6% indicated that the transition occurs within the interval between Re=150 and Re=200. The simulated 3-D flow at Re=150 ($A=6$, case 2 in Table I) did not exhibit any sign of spanwise variation, i.e., the flow was completely two dimensional. In addition, when using the same cross-sectional grid as well as other numerical parameters, the 3-D simulation at this Re reproduced the same fully developed flow as in the 2-D simulation (case 1). Consequently, the global results were identical for these cases; see Table I. In contrast, the simulated 3-D flows at Re=200 (cases 4 and 5) both evolved, after some initial period of regular 2-D shedding flow, into a condition of a transition to 3-D flow. In these 3-D simulations, the regular but transient 2-D shedding flow was identical to the flow produced by the corresponding 2-D simulation (case 3). In Fig. 4, for an aspect ratio of $A=6$ (cases 4, 7 and 10; Re =200, 250, and 300), the time evolution of spanwise-averaged lift and drag (left) are depicted together with some spanwise variations of sectional drag in the fully developed state (right). In the case of Re=200; see Fig. 4(a) and Fig. 7(a), the initial period of fully two-dimensional flow extended up to $t=180-200$, after which there was a transition to three-dimensional flow. During this transition process, there was a drop in drag level, lift amplitude, and shedding frequency. The scenario bears strong resemblance to the CC flow simulations of Henderson[3] at around the subcritical bifurcation to mode A.

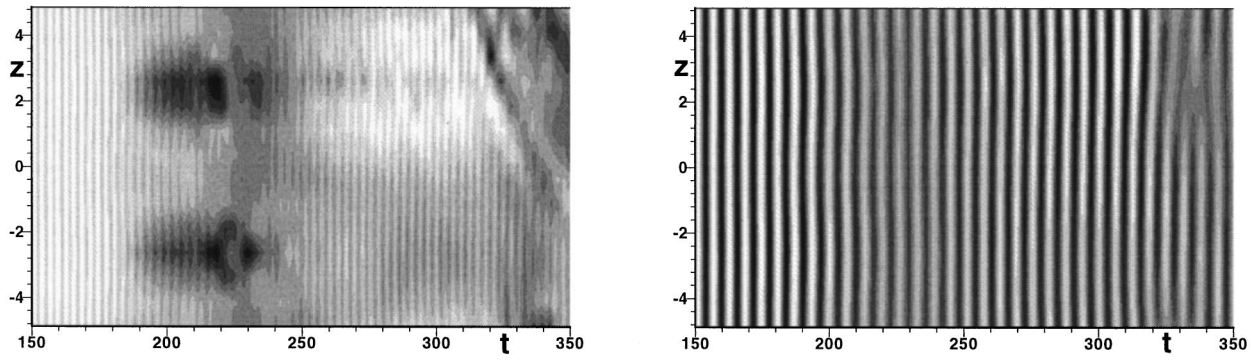

FIG. 8. Isocontours of (a) drag and (b) lift coefficients versus time and the spanwise position for (Re=200, $A=10$). For C_D, black corresponds to $C_D=1.26$ and white to $C_D=1.48$. For C_L, black corresponds to $C_L=-0.45$ and white to $C_L=0.45$.

D. Force pulsations

The stationary 3-D flow for Re$\leqslant$300 exhibited a marked and characteristic pulsation (or bursting) in the force components; see Figs. 4 and 7. The instants of maximum force level appeared to be random in time, although there seemed to be a preference to a pulsation rate corresponding to 10–16 mean shedding periods (60–100 time units) for Re=200, 250. While this is not conclusive, there was a slight tendency for the pulsations to occur more frequently at $A=6$ compared to $A=10$ (Re=200, 250); see Figs. 4 and 7. With increasing Re, the pulsations faded out to be completely absent at Re$\geqslant$400; see Fig. 5 (left). Hereafter, these characteristic time periods with high and low levels of forces are referred to as HF and LF regions, respectively.

The present simulations indicated that the spanwise coupling of forces and the associated near-wake flow components were higher in HF regions than in LF regions. Spanwise variations of the sectional drag coefficient for Re=200, 250, 300 ($A=6$) are shown on the right in Fig. 4. As an example, for Re=200 at $t=600$, see Fig. 4(a), which is located within an LF region, the spanwise variations of the sectional drag are substantial, whereas, at $t=650$, which is located within an HF region, these variations are almost negligible. A similar behavior can be seen for Re=250 [Fig. 4(b)]. However, at Re=300 [Fig. 4(c)], the distinction between LF and HF regions, owing to spanwise coupling is not very evident from the spanwise variation of sectional drag (e.g., $t=410$, which is within an HF region). For these Re, as evidenced below (Sec. V E), the near-wake flow has already developed a significant degree of three-dimensionality, which might mask the proposed increased spanwise coupling associated with the HF regions. Nevertheless, the phenomenon of pulsations was not present for Re>300.

E. Couplings between shedding frequency and lift amplitude

The coupling between the instantaneous shedding frequency, f_L, as deduced from the lift signal, and the instantaneous lift envelop amplitude A_L, was investigated for different Reynolds numbers (3-D simulations). In Fig. 7, the time evolutions of A_L and f_L are shown together with the force coefficient $C_F=\sqrt{C_D^2+C_L^2}$ for Re=200 and Re=250 ($A=10$), respectively. In the stationary flow condition, the cross-correlation coefficient between A_L and f_L with a variable time delay was calculated. The cross-correlation was based on signals of A_L and f_L, as determined from the Hilbert transform,[38] whereas the somewhat smoother but otherwise identical variations shown in Fig. 7 were taken directly from the instants of peak lift amplitudes. For each case, the extreme cross-correlation value (either positive or negative)

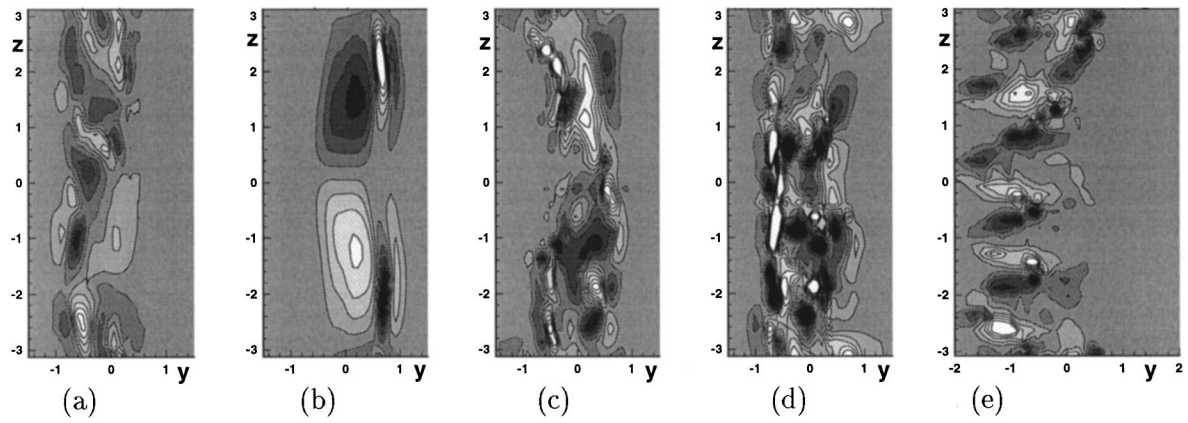

FIG. 9. Streamwise vorticity (ω_x) contours in plane $x=2$ for $A=6$. (a) Re=200, $t=379$ (LF region), $\Delta\omega_x=0.4$; (b) Re=200, $t=554.5$ (HF region), $\Delta\omega_x=0.2$; (c) Re=250, $t=375$, $\Delta\omega_x=0.4$; (d) Re=300, $t=375$, $\Delta\omega_x=0.4$; (e) Re=500 (case 15), $t=231.5$, $\Delta\omega_x=1$.

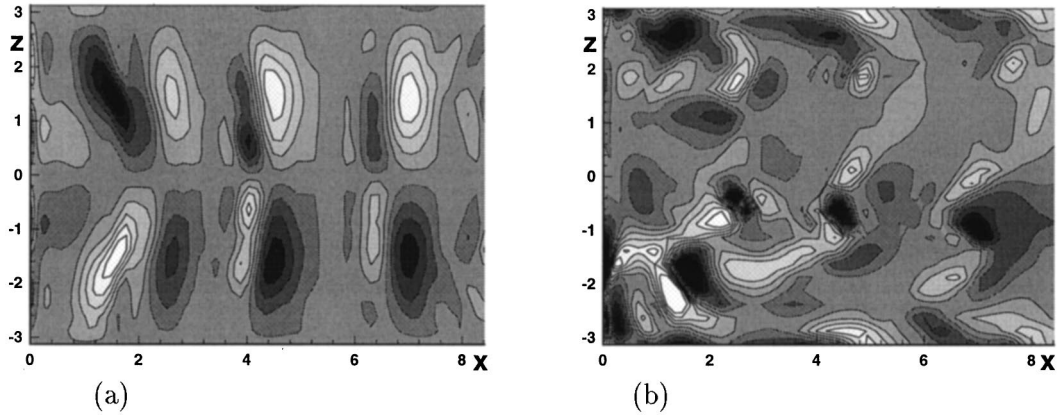

FIG. 10. Cross-stream vorticity (ω_y) contours in plane $y=0$ for Re=200, $A=6$. (a) HF region ($t=329$, $\Delta\omega_y=0.09$); (b) LF region ($t=598$, $\Delta\omega_y=0.2$).

and its associated time delay were recorded. For Re$\leqslant$300, the extreme values were positive with a time delay corresponding to the lift frequency leading the lift amplitude, while the opposite was true for Re$>$300. There was thus an apparent change in the character of coupling occurring between Re=300 and Re=400. As noted earlier, the force pulsations disappeared between these Re. The suggestion is that the initial transition process from 2-D to 3-D flow is completed at around a Re close to but higher than Re=300. A simple interpolation based on the the extreme values of the cross-correlation suggested that the changeover occurred at Re$\approx$340. Interestingly, a negative coupling between frequency variations and lift-related signals, as for Re$\geqslant$400 in this study, is reported in CC flow within the upper subcritical regime (approximately $5\times10^3<\mathrm{Re}<2\times10^5$).[39]

The high degree of (positive) coupling between frequency and lift amplitude for low Re is illustrated in Fig. 7, where it is also evident that the variations in shedding frequency lead the variations in lift amplitude (by about two shedding periods). It is of interest to note that the initial drop in frequency at the onset of 3-D flow for Re=200 also occurred prior to the drop in force level (by about two to three shedding periods).

F. Wake vorticity structures

At Re=150, the wake was laminar, completely two dimensional, and characterized by the primary instability, the von Kármán vortices. At higher Reynolds numbers (Re$\geqslant$200), the wake became inherently three dimensional and complex, showing ingredients of spanwise secondary (mode A and B) instability structures, similar to the wake behind a circular cylinder.

This section continues with a short overview on wake vorticity structures within the planes $x=2, y=0$, and $z=0$. Vorticity contours are shown in Figs. 9–13. In all vorticity plots, the zero-centered grey scale was divided into ten levels (interval steps are indicated within the figure captions). As a crude measure of the intensity of secondary vortices, which were primarily oriented in the streamwise direction, the streamwise circulation, Γ_x, was calculated at $x=2$ within the region $y\in(-2,2)$ across the span. Time sequences of Γ_x are shown in Figs. 14 and 15.

Streamwise vorticity contours in plane $x=2$, for Re =200 at $t=379$ and $t=554.5$, are shown in Figs. 9(a) and 9(b), respectively. These two instants are located within LF and HF regions, respectively; see also Figs. 4 and 14. At t

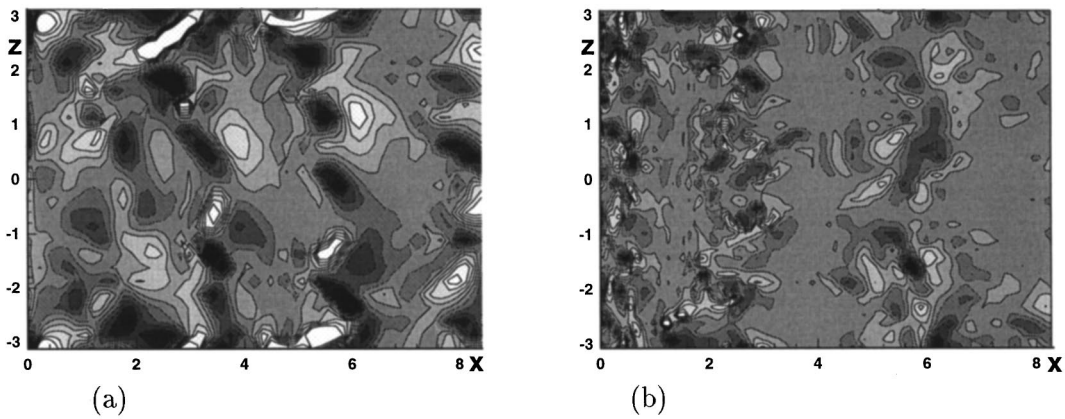

FIG. 11. Cross-stream vorticity (ω_y) contours in plane $y=0$ for $A=6$. (a) Re=250 ($t=329$, $\Delta\omega_y=0.2$), (b) Re=500 (case 15, $t=221$, $\Delta\omega_y=0.8$).

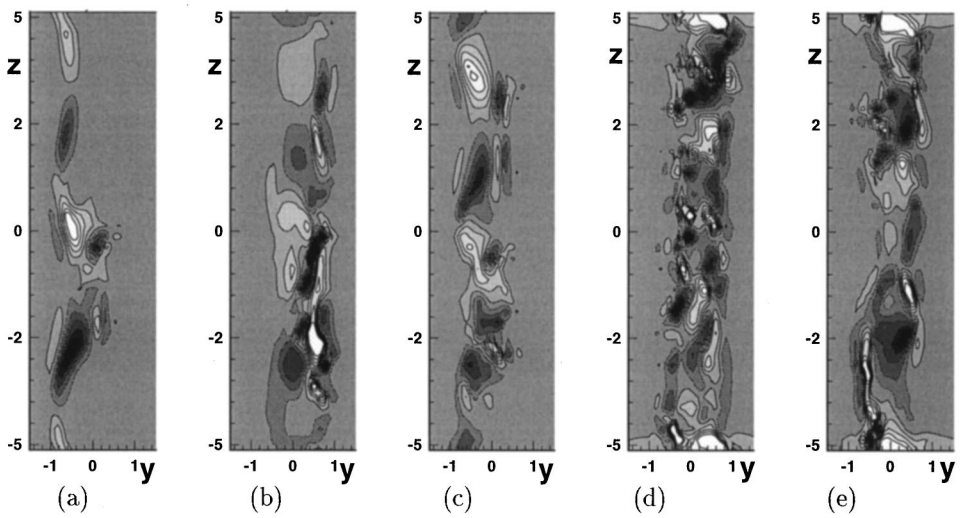

FIG. 12. Streamwise vorticity (ω_x) contours in plane $x=2$ for $A=10$, $\Delta\omega_x=0.4$. (a) Re=200 (HF region); (b) Re=200 (LF region); (c) Re=200 (HF region); (d) Re=250 ($t=404$); (e) Re=250 ($t=410$).

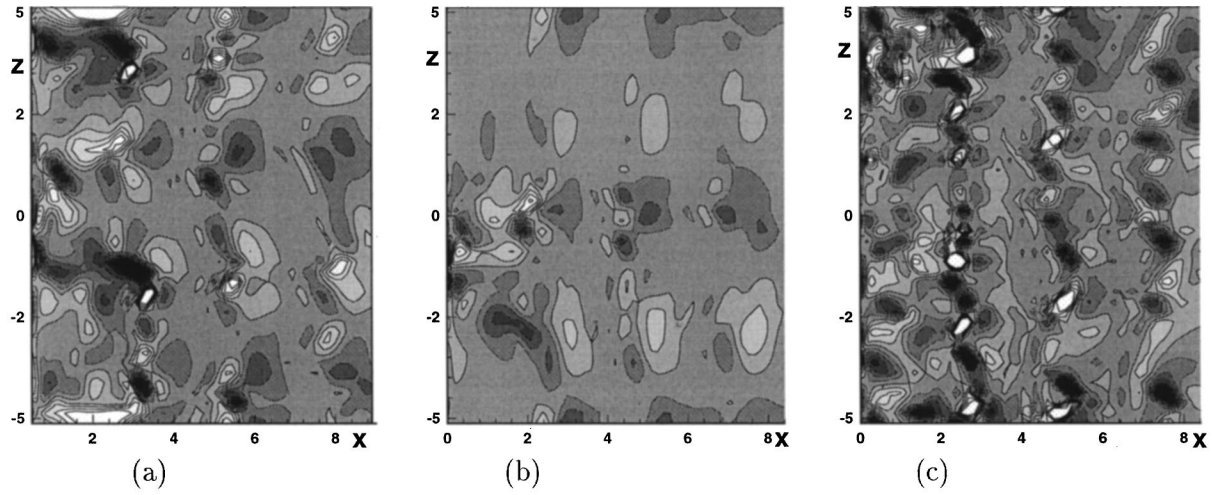

FIG. 13. Cross-stream vorticity (ω_y) contours in plane $y=0$ for $A=10$, $\Delta\omega_x=0.2$. (a) Re=200 (LF region); (b) Re=200 (HF region); (c) Re=250 ($t=535$).

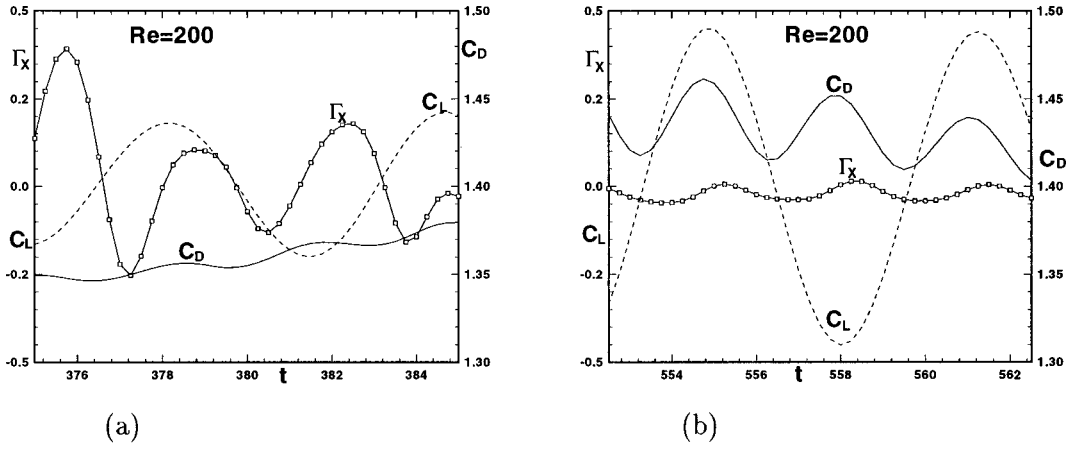

FIG. 14. Streamwise circulation Γ_x in plane $x=2$ together with spanwise-averaged lift and drag coefficients versus time for Re=200, $A=6$. (a) LF region; (b) HF region. The circulation is calculated in the domain $y\in(-2,2)$, $z\in(-3,3)$.

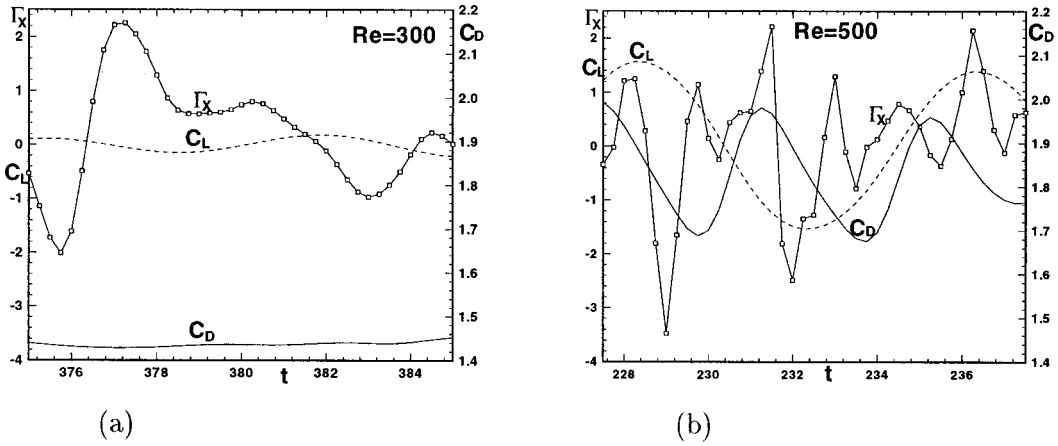

FIG. 15. Streamwise circulation Γ_x in plane $x=2$ together with spanwise-averaged lift and drag coefficients versus time for $A=6$. (a) Re=300; (b) Re=500 (case 15). The circulation is calculated in the domain $y\in(-2,2)$, $z\in(-3,3)$.

$=554.5$, an ordered cluster of secondary vortical elements with an alternating sign variation is visible. They seem very regular and change their sign repeatedly in the z direction.

At this particular instant, the dominating spanwise wavelength is about three diameters. The corresponding behavior for ω_y in the wake centerplane ($y=0$) at $t=329$, also within an HF region, is shown in Fig. 10(a). Evidently, for these large-scale structures, there is also a sign periodicity in the x direction, although the periodicity is not perfectly regular. Moreover, at a given position in the planes $x=2$ and $y=0$, a periodicity in time was also observed, especially within the HF regions. The vorticity structures as described above are similar to the mode A type of instabilities that are present in transitional CC flow; see, e.g., Refs. 1, 3, 11, 18, and 40. By increasing the computational aspect ratio from 6 to 10, similar structures, as for $A=6$, especially within HF regions, also existed for $A=10$; see Figs. 12(a), 12(c) and 13(b). It should be emphasized that, within the so-called HF regions, the secondary flow structures were not always as clean and regular as indicated, e.g., from Figs. 9(b) and 10(a), especially not so for the higher computational aspect ratio $A=10$; see, e.g., Figs. 12(a), 12(c), and 13(b). At $t=379\,(A=6)$ in Fig. 9(a), $t=598\,(A=6)$ in Fig. 10(b) and $t=587\,(A=10)$ in Fig. 13(a), which all are within a LF region, the appearance of the secondary vortices were highly irregular and chaotic and also had significantly higher peak vorticity levels.

Referring to Fig. 14, which is for Re=200, it is observed that, within HF regions (right), the time variations of Γ_x in plane $x=2$ are very small, whereas the opposite is true within LF regions (left). Similar variations as are shown in Fig. 14 were also obtained at other time intervals and for other distances downstream of the cylinder ($x=3$ and $x=4$). As shown in Fig. 14, the time variations of Γ_x were closely connected to the variations in the spanwise-averaged drag coefficient. The intensity of streamwise vorticity (as monitored, e.g., from peak values in ω_x) and the streamwise circulation, Γ_x, increased with an increasing Reynolds number. For example, the amplitudes of Γ_x were approximately ±0.2, ±0.5, ±2, and ±3 for Re=200, 250, 300, and 500, respectively; see Figs. 14 and 15. Although not monitored rigorously, the corresponding changes in spanwise circulation associated with the individual von Kármán vortices at their formation appeared to be much smaller. Nevertheless, the intensity of these vortices (as monitored from near-wake peak values in ω_z) increased with an increase in Re.

For Re$\geqslant$250, another type of secondary vortices with a spanwise periodicity of the order of one cylinder diameter were observed. The character of these vortices was similar to the mode B instability structures, as found in CC flow.[1,3,11] In Fig. 11(a) for $A=6$ and in Fig. 13(c) for $A=10$, both at Re=250, signs of these vortices intersecting the plane $y=0$ along rows $x\simeq$const, are visible. At Re=500, vortical structures similar to both modes A and B were observed, but they appeared much more more chaotic as compared with lower Re (e.g., at Re=250). In this case (Re=500), the spanwise wavelength within each (staggered) array of longitudinal vortices, intersecting the plane $y=0$ at different positions, varied from about one diameter in the near-wake to approximately four diameters farther downstream, in the intermediate wake; see, e.g., Figs. 9(e) and 11(b). Presumably, as demonstrated in Henderson,[3] the mode B vortices are dominant within a region close to the cylinder while there is a mixed A–B state within regions more downstream; also see Zhang *et al.*[18] In closing this section, it should be emphasized that the above descriptions were based on vorticity fields in the stationary flow condition.

G. Results for Re=500

Spanwise vorticity contours for Re=500 (case 15) are shown in Fig. 16. As is evident, the simulated vortex shedding was extremely powerful at this Re. In Fig. 16(b), which is at an instant of minimum lift, there is a very strong von Kármán vortex peeling off from the lower side of the cylinder (in white). At position ($x\simeq1, y\simeq0$) within this vortex, the spanwise vorticity has its maximum value ($\omega_z=7.6$). For the vortex on the upper side (in black), which is still connected to the cylinder, the extreme spanwise vorticity is $\omega_z=-7.5$ at position $x\simeq2.4, y\simeq-0.3$. At this extreme instant, the angle of the projected force vector is about 43° from the wake centerline (pointing downward). At this Re, significant levels in components of nonspanwise vorticity were present

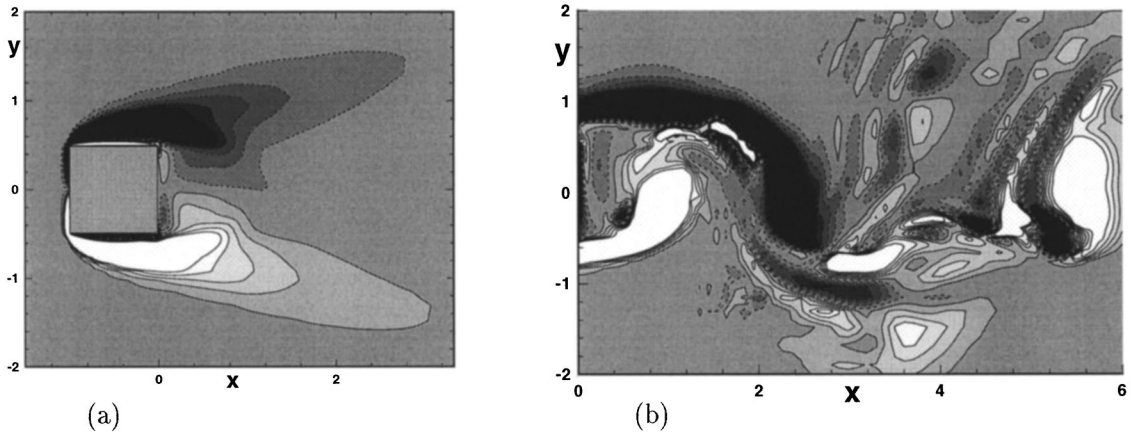

FIG. 16. Spanwise vorticity contours (ω_z) at midspan for Re=500 (case 15). Here $\Delta\omega_z=0.4$, solid lines $\omega_z>0$. Left: time-averaged. Right: $t=240$ (the instant of minimum lift).

close to the cylinder. For instance, at the positions of extreme ω_z given above the levels in $\sqrt{\omega_x^2+\omega_y^2}$ were 2.4 and 3.7, respectively. At the instant shown in Fig. 16(b), there are also signs of secondary mode B structures. For instance, starting off within the braid region between the two above spanwise vortices and below the second one, there is a curved tubular (type B) structure that is evidently generated very close to the cylinder, in the near-wake region. Within this structure, $\sqrt{\omega_x^2+\omega_y^2}$ reached a level of about 7.5 ($x\simeq 2.0, y\simeq -0.4$). Due to the powerful shedding (wake swinging) and the presence of these tubular structures as well as other small-scale vortical flow elements, the intermediate wake has a very complex vortical structure.

Figure 17 shows the mean pressure coefficient over the body and the mean pressure coefficient and velocity along the wake centerline of wake. No experimental or numerical results for Re=500 were found for comparison. Nonetheless, there are some similarities with laminar (Re=150) and fully turbulent flow conditions for the pressure coefficient over the body, as exemplified by the inserted experimental data for $\mathrm{Re}=5\times10^3$; see Ref. 26. On comparing results for Re=150 (case 1) and Re=500 (case 15), it is observed that the base pressure coefficient (C_{pb}), the minimum pressure coefficient ($C_{p,\min}$), and the mean length of the recirculating region behind the body (L_r) decrease with increasing Re. The values change from $C_{pb}=-0.74, C_{p,\min}=-0.90$, and $L_r=1.77$ at Re=150 to $C_{pb}=-1.24, C_{p,\min}=-1.64$, and $L_r=0.59$ at Re=500. As indicated from the variation in the mean drag coefficient; see Fig. 3(b), there is a steady decrease in C_{pb} with increasing Re from about Re=200. For higher Re, measured data (Okajima and Sugitani[41] and the unpublished results of Norberg[42]) reveal that C_{pb} decreases to a local minimum at around $\mathrm{Re}=2\times10^3$, where $C_{pb}\approx-1.55$ (for $\mathrm{Re}=5\times10^3$, $C_{pb}\simeq=-1.47$; see Fig. 17).

VI. DISCUSSION

A. Transitional flow

For the flow around a circular cylinder (CC flow), as described in Henderson and Barkley[11] and Henderson,[3] there exists a band of unstable spanwise mode A wavelengths above the onset Re for three-dimensionality. When the spanwise dimension, the computational aspect ratio, is larger than or comparable to the largest unstable wavelength, it can be expected that the flow will exhibit elements of spatiotemporal chaos as a result of nonlinear interactions within this band of wavelengths (competition between modes).[3] It seems that similar to CC flow, there exists such a band of unstable mode A wavelengths in SC flow as well. The precise extent of this band could not be determined from the present simulations. Unfortunately, no flow field sequences during early stages of the wake instability, i.e. at around the initial drop in force level, were recorded. In CC flow, this seems to be the best time period for finding the spanwise extent corresponding to

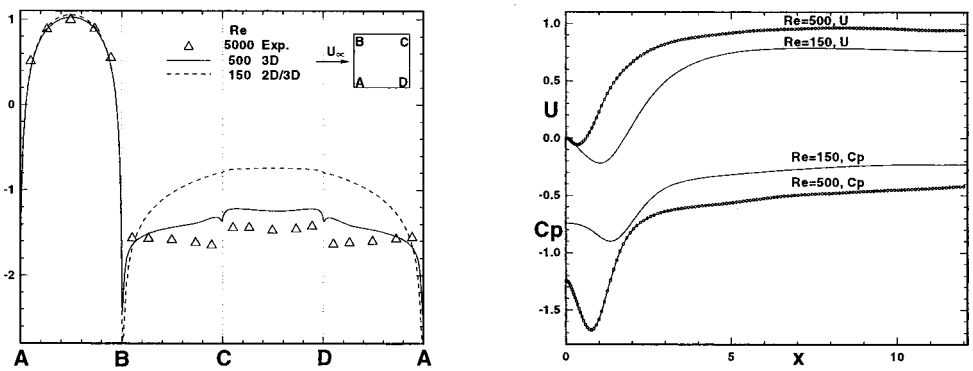

FIG. 17. The pressure coefficient over the cylinder surface (left) and pressure coefficient and streamwise velocity along the wake centerline $y=0$ (right); time- and spanwise-averaged results.

the maximum growth rate.[19] However, for all 3-D cases (except case 14), the complete sequences of temporal variation of sectional drag and lift across the span were recorded. The spanwise–temporal variations of C_D and C_L for (Re=200, $A=10$) between $t=150$ and $t=350$ are depicted by isocontours in Fig. 8. As is evident from Fig. 8 (left), the transitional (2-D/3-D) drop in force level at around $t=190$, see Fig. 7(a), is associated with a blob-like three-dimensional disturbance having a spanwise periodicity of approximately five diameters. For (Re=200, $A=6$) a similar transitional behavior was found, the exception being that the wavelength was instead approximately six diameters. These two wavelengths seem to be directly related to the actual computational spanwise dimension. Presumably, assuming the initial disturbance to be perfectly sinusoidal in the spanwise direction, the imposed spanwise periodic boundary condition forces the simulation to pick out not exactly the most unstable wavelength (as can be deduced, e.g., from a Floquet analysis[11]) but some nearby wavelength (within the assumed band of unstable wavelength), which is compatible with the actual spanwise dimension. For Re=200, the 2-D/3-D transitional drop in shedding frequency and force level occurred approximately ten time units earlier with $A=10$ as compared to $A=6$, indicating that the five diameter wavelength is the most unstable one between the two. There was no indication of a slanted shedding behavior in connection with the 2-D/3-D transition.

The pulsations (LF and HF regions) were believed to be part of the initial process of transition from 2-D to 3-D flow. As explained in Henderson,[3] the three-dimensional mode A, which is initiated at the first transition from 2-D to 3-D flow, is strongly connected to the two-dimensional shedding wake, the primary instability. As is evident from Figs. 4(a) and 7(a) for Re=200, the level of forces and Strouhal number within HF regions are close to their two-dimensional counterparts (within the initial transient region). With a subsequent increase in Re, the distance from the transitional Re increases, which is evidently connected to the fade out of the pulsation phenomenon. It can thus be expected that the presence of pulsations is related to some coupling mechanisms between the primary two-dimensional instability (the von Kárman shedding) and secondary mode A instabilities. In CC flow experiments, the wake transition regime (approximately $185<\mathrm{Re}<260$); see, e.g., Williamson,[19] it was noted that the wake flow locally exhibits intermittent amplitude modulations. The interpretation in Ref. 16 is that these modulations are caused by the presence of large-scale ''dislocation'' structures that intermittently fill out a large region of space as they spread out downstream. In Henderson,[3] the same structures are referred to as ''spot-like'' disturbances, and the interpretation is that their appearance results from the growth of subdominant instability modes. It is uncertain whether these structures will cause any significant pulsation in the spanwise-averaged forces on the cylinder. In previous 3-D simulations of transitional CC flow; e.g., see Refs. 3, 18, 35–37, 43, there has been no evidence put forward on distinct force pulsations similar to these found in the present study. However, a recent DNS simulation by Balachandar *et al.*[44] for a normal flat plate at Re=250 did exhibit pulsations strongly resembling the present ones (no explanation is provided). In Henderson,[3] a force pulsation (modulation) behavior is observed in simulations for Re=1000 in CC flow, in particular, at large computational aspect ratios. These modulations appear as a result of large-scale phase dislocations in the near wake. The suggested origin in Ref. 3 is that the phase dislocations are caused by the competition between low wave number spatial (spanwise) modes in the wake. As monitored from spanwise–temporal lift variations, occasional (actually only three events in total) phase dislocations of the von Kármán vortices were indicated, but only when the larger spanwise dimension was used ($A=10$). For Re=200, one such dislocation occurred at $t\simeq335$; see Fig. 8 (right). For Re=250, one occurred at $t\simeq380$ and one at $t\simeq500$, the last one causing the spanwise-averaged lift amplitude to drop practically to zero; see Fig. 7(b). Evidently, these occasional phase dislocations cannot explain the occurrence of force pulsations.

As is shown in Fig. 7, at transitional Reynolds numbers Re=200 and Re=250, the shedding frequency variations lead the corresponding variations in the lift envelope amplitude. This interesting feature might be related to a redistribution or formation process of transitional wake flow elements along the span, which is presumably a much slower process compared to the roll-up of the primary von Kármán vortices (the shedding frequency is primarily governed by the primary 2-D instability without any new time scale introduced from the secondary 3-D structures[3]). As suggested in Henderson,[3] the initial drop in both force level and shedding frequency is due to the three-dimensional distortions of the primary vortices by strong nonlinear interactions with the 3-D instability. That the frequency leads may then be related to the fact that the mode A instabilities are initiated at a position somewhat downstream in the wake, with a subsequent rapid effect on the shedding frequency, and that it then takes some time for the flow distortion effects to propagate upstream and finally reach the cylinder. Interestingly, in Henderson,[3] for a simulated CC flow at a Re slightly above onset (Re=195, $\mathrm{Re}/\mathrm{Re}_{c2}-1\simeq0.04$) and for $A=3.96$ (corresponding to the onset wavelength of mode A), there is no phase shift between the shedding frequency and lift amplitude at the initiation of three-dimensional flow.

The phase shift found in the present simulations suggests some fundamental differences between CC and SC flow concerning the transitional process. It is suggested that the force pulsations that were present in the present simulations are related to this phase shift. On occasions probably scaling with the initial time delay itself, the flow will pulsate between an ordered state with a domination from the primary instability, with subsequent growth of unstable mode A instabilities and a state in which there is a chaotic mix of such spanwise 3-D instabilities with substantial deformations of the primary instability. In CC flow there might be some feedback mechanism that locks the phase between the primary instability and the deformations due to the secondary instabilities.

Transient simulations at Reynolds numbers within the stable laminar shedding regime, e.g., for Re=100, show that the saturation process toward the stationary flow condition,

in which the lift amplitude increases with time, involves an associated increase in the shedding frequency; see, e.g., Schumm *et al.*[7] With an increase in aspect ratio from $A=6$ to $A=10$ (Re=200, 250) there was a decrease in the strength of the positive coupling between lift amplitude and shedding frequency. As stated in Henderson,[3] an increase in the spanwise dimension ''leads to spatiotemporal chaos driven by the competition between multiple self-excited mode A instabilities.'' This competition of mode A instabilities, together with the suggested link to the primary instability, causing force pulsations, is then in accordance with the observed decrease in positive coupling for Reynolds numbers between the onset from 2-D to 3-D flow and Re=300, approximately. At larger aspect ratios, the increasing complex interactions within the band of unstable spanwise mode A wavelengths will, to some degree, reduce the positive coupling. However, as $A=10$ at Re=200, 250 is probably well above the maximum unstable mode A wavelength at which it can be expected that the positive coupling is an intrinsic feature of the initial transitional process.

Thus, although many features associated with the transition from 2-D to 3-D flow appear to be similar to CC flow, e.g., the presence of mode A and B instabilities, the presence of distinct force pulsations in flow around bodies with sharp edges seem to be dissimilar to CC flow.

B. Beyond the 2-D/3-D wake transition

With increasing Re between Re=250 and Re=500, there was a substantial increase in the intensity of the near-wake secondary vortical structures (an approximate six-fold increase in the streamwise circulation level in the plane $x=2$ was indicated). At Re=500, these secondary vortices were primarily of the mode B type. The intensity of the von Kármán vortices increased as well, but the variations indicated were significantly smaller. From experiments on the flow around a circular cylinder (CC flow); see Brede *et al.*;[40] the increase in near-wake streamwise circulation between Re=250 and Re=500 seems to be much smaller. The force pulsations disappeared between Re=300 and Re=400. Interestingly, for Re$\geqslant$300, there was an indicated large increase in the spanwise correlation of lift forces (with increasing Re). The coupling between an increased intensity of mode B structures and a higher spanwise correlation can be understood from the following citation from Henderson:[3] the growth of mode B causes a large reduction in the amplitude of mode A, driving the system back toward a ''two-dimensional state.'' However, more investigations are needed to clarify the apparent large increase in spanwise correlation.

On comparison of variations in Strouhal number and mean drag coefficient with Reynolds number, when comparing SC and CC flow for $250\leqslant Re\leqslant 2\times 10^3$ approximately, a different trend of changes can be observed; see Fig. 3. In SC flow, the Strouhal number decreases and the mean drag coefficient increases with Reynolds number, whereas the opposite trends are valid for the circular cylinder; see, e.g., Refs. 3 and 20. These opposite trends, when comparing CC and SC flow, may be a result from some fundamental differences in the separation process. In present study previous[8,13] findings regarding the separation process in SC flow are confirmed and extended. For all Reynolds numbers (Re=150–500), separation occurred at all times from the upstream corners. For Re=150, which in the present study means completely two-dimensional shedding flow, the flow was at all times also attached to either the upper or the lower wall (within the downstream half), with a subsequent separation from the following downstream corner. For Re=200, with inherently three-dimensional shedding flow, reattached flow was absent. However, on occasion, the flow was rather close to reattachment at downstream corners. For Re$\geqslant$250, the cross-stream size of the fully separated region, the wake width, increased with an increase in Re. Consequently, at these Re, the separation line is straight and independent of time, whereas for the circular cylinder, owing to the alternate shedding, the position of separation fluctuates with time.[14] Moreover, the post-transitional and turbulent shedding flow exhibits relatively strong inherent three-dimensional effects, and this may cause undulations of the separation line for the circular cylinder, but not for the square cylinder. In fact, at these Reynolds numbers, undulations of the separation line for the circular cylinder are described by Yokoi and Kamemoto[45,46] For CC flow, from about Re=300 to $Re=1.5\times 10^3$, there is a decrease in the spanwise correlation related to the fluctuating lift forces (Norberg[47]). The present simulations indicated that spanwise correlation of sectional lift forces increases with increasing Re$\geqslant$300. From the studies of Yokoi and Kamemoto,[45,46] the undulation of the separation line seems to be related to the longitudinal, mode B type, vortical tube structures that are present in the near wake. As shown in Williamson,[1] the mode B vortical structures are influenced by the reverse flow of the circular cylinder wake. It may then be that the difference as compared with CC flow is related to the fact that the secondary structures cannot affect the undulation of the separation line in SC flow. For CC flow, however, the secondary structures may interact with the separation process, and this anticipated feedback mechanism presumably causes a reduction in mode B circulation and, consequently,[3] a reduction in the spanwise correlation of the von Kármán vortices, which are primarily responsible for the fluctuations in lift, the drag level, and the shedding frequency.

VII. CONCLUSIONS

The 2-D and 3-D unsteady flow simulations past a square cylinder at zero incidence (flat face facing the flow) at moderate Reynolds numbers (Re=150–500) and for a solid blockage of $\beta=5.6\%$ were carried out. In 3-D simulations, the computational spanwise length was six diameters. However, for Re=200, 250, a spanwise length of ten diameters was also investigated, with small to negligible effects on the global results.

The simulations indicated a stable 2-D laminar shedding flow at Re=150, whereas effects of three-dimensional flow appeared at Re=200. At this Re, the spanwise wavelength associated with the initiation of transition from 2-D to 3-D

flow, as deduced from spanwise–temporal variations in the cylinder drag, was found to be approximately five diameters.

The 2-D results for mean drag were in reasonable agreement with experiments although other quantities and flow characteristics for $Re \geqslant 200$ were, for the most part, in sharp contrast to available experimental data and the present 3-D results. The spectra of fluctuating lift and drag from two-dimensional simulations and for $Re \geqslant 300$ exhibited a scenario of period doublings. Period doublings were not present in the three-dimensional simulations. With respect to blockage effects and experimental uncertainties, the 3-D results were in general agreement with experimental data (only available for the Strouhal number and mean drag).

For $Re=200$, 250, 300 (3-D simulations) the forces on the cylinder exhibited a marked and characteristic pulsation in time. The instants of the maximum force level appeared to be random in time, although, for $Re=200$, 250, there seemed to be a preference toward a pulsation rate corresponding to 10–16 mean shedding periods (60–100 time units). Associated with the presence of force pulsations, there was a time-shifted positive coupling between the instantaneous shedding frequency and the lift amplitude, with shedding frequency leading the amplitude. In the time regions of high force levels, the flow was in an ordered state with relatively small spanwise variations whereas, in low-force regions, the three-dimensional effects were strong with a seemingly chaotic spanwise flow structure. The pulsating forces, especially the drag, were closely related to the activity of the secondary vortices.

Vortical structures similar to the spanwise mode A type of wake instabilities, as found in flow around circular cylinders, were present, especially in connection with time regions of high forces. The spanwise wavelength of these instabilities were predominantly between two and five diameters. For $Re \geqslant 250$, structures similar to the mode B wake instability, with a dominant wavelength of about one diameter, were also present.

For $Re \geqslant 300$, the indicated spanwise coupling of lift forces increased with increasing Re. In particular, for $Re=500$, an extremely high spanwise correlation of lift forces was indicated.

[1] C. H. K. Williamson, ''Vortex dynamics in the cylinder wake,'' Annu. Rev. Fluid Mech. **28**, 477 (1996).

[2] A. Okajima, ''Numerical analysis of the flow around an oscillating cylinder,'' in *Proceedings of the 6th International Conference on Flow-Induced Vibration*, edited by P. W. Bearmen, London, UK, 10–12 April 1995, Balkema, Rotterdam, pp. 1–7.

[3] R. D. Henderson, ''Nonlinear dynamics and pattern formation in turbulent wake transition,'' J. Fluid Mech. **352**, 65 (1997).

[4] M. Coutanceau and R. Bouard, ''Experimental determination of the main features of the viscous flow in the wake of a circular cylinder in uniform translation, Part 1. Steady flow,'' J. Fluid Mech. **79**, 231 (1977).

[5] M. Provansal, C. Mathis, and L. Boyer, ''Bénard–von Kármán instability: Transient and forced regimes,'' J. Fluid Mech. **182**, 1 (1987).

[6] C. P. Jackson, ''A finite-element study of the onset of vortex shedding in flow past variously shaped bodies,'' J. Fluid Mech. **182**, 23 (1987).

[7] M. Schumm, E. Berger, and P. A. Monkewitz, ''Self-excited oscillations in the wake of two-dimensional bluff bodies and their control,'' J. Fluid Mech. **271**, 17 (1994).

[8] A. Sohankar, C. Norberg, and L. Davidson, ''Numerical simulation of unsteady flow around a rectangular two-dimensional cylinder at incidence,'' J. Wind Eng. Ind. Aero. **69**, 189 (1997).

[9] A. Sohankar, C. Norberg, and L. Davidson, ''Low-Reynolds number flow around a square cylinder at incidence: Study of blockage, onset of vortex shedding and outlet boundary condition,'' Int. J. Numer. Methods Fluids **26**, 39 (1998).

[10] K. M. Kelkar and S. V. Patankar, ''Numerical prediction of vortex shedding behind a square cylinder,'' Int. J. Numer. Methods Fluids **14**, 327 (1992).

[11] D. Barkley and R. D. Henderson, ''Three-dimensional Floquet stability analysis of the wake of a circular cylinder,'' J. Fluid Mech. **322**, 215 (1996).

[12] A. Roshko, ''On the development of turbulent wakes from vortex streets,'' NACA Report 1191, National Advisory Committee for Aeronautics, 1954.

[13] A. Sohankar, L. Davidson, and C. Norberg, ''Numerical simulation of unsteady flow around a square two-dimensional cylinder,'' in *12th Australasian Fluid Mechanics Conference*, 10–15 December 1995, Sydney University, Sydney, Australia, 1995, pp. 517–520.

[14] R. Franke, W. Rodi, and B. Schönung, ''Numerical calculation of laminar vortex-shedding flow past cylinders,'' J. Wind Eng. Ind. Aero. **35**, 237 (1990).

[15] C. H. K. Williamson. ''The existence of two stages in the transition to three-dimensionality of a cylinder wake,'' Phys. Fluids **31**, 3165 (1988).

[16] C. H. K. Williamson, ''The natural and forced formation of spot-like ''vortex dislocations'' in the transition of a wake,'' J. Fluid Mech. **243**, 393 (1992).

[17] B. R. Noack, M. König, and H. Eckelmann, ''Three-dimensional stability analysis of the periodic flow around a circular cylinder,'' Phys. Fluids A **5**, 1279 (1993).

[18] H. Zhang, U. Fey, B. R. Noack, M. König, and H. Eckelmann. ''On the transition of the cylinder wake,'' Phys. Fluids **7**, 779 (1995).

[19] C. H. K. Williamson, ''Three-dimensional wake transition,'' J. Fluid Mech. **328**, 345 (1996).

[20] C. Norberg, ''An experimental investigation of the flow around a circular cylinder: influence of aspect ratio,'' J. Fluid Mech. **258**, 287 (1994).

[21] L. Davidson, ''LES of recirculating flow without any homogeneous direction: A dynamic one-equation subgrid model,'' in *2nd International Symposium on Turbulence Heat and Mass Transfer*, Delft, 1997, Delft University, pp. 481–490.

[22] P. Emvin, ''The full multigrid method applied to turbulent flow in ventilated enclosures using structured and unstructured grids,'' Ph.D. thesis, Chalmers University of Technology, Gothenburg, April 1997.

[23] J. S. Bendat and A. G. Piersol, *Random Data: Analysis and Measurement Procedures* (Wiley-Interscience, New York, 1971).

[24] S. C. Kacker, B. Pennington, and R. S. Hill. ''Fluctuating lift coefficient for a circular cylinder in cross flow,'' J. Mech. Eng. Sci. **16**, 215 (1974).

[25] R. Mittal and S. Balachandar, ''Effect of three-dimensionality on the lift and drag of nominally two-dimensional cylinders,'' Phys. Fluids **7**, 1841 (1995).

[26] C. Norberg, ''Flow around rectangular cylinders: pressure forces and wake frequencies,'' J. Wind Eng. Ind. Aero. **49**, 187 (1993).

[27] R. W. Davis and E. F. Moore. ''A numerical study of vortex shedding from rectangles,'' J. Fluid Mech. **116**, 475 (1982).

[28] R. W. Davis, E. F. Moore, and L. P. Purtell, ''A numerical-experimental study of confined flow around rectangular cylinders,'' Phys. Fluids **27**, 46 (1984).

[29] M. P. Arnal, J. A. C. Goering, and D. J. Humphrey, ''Vortex shedding from a bluff body adjacent to a plane sliding wall,'' Trans. ASME: J. Fluids Eng. **113**, 384 (1991).

[30] G. Li and J. A. C. Humphrey, ''Numerical modeling of confined flow past a cylinder of square cross-section at various orientations,'' Int. J. Numer. Methods Fluids **20**, 1215 (1995).

[31] A. Okajima, ''Strouhal numbers of rectangular cylinders,'' J. Fluid Mech. **123**, 379 (1982).

[32] A. Okajima (personal communication, 1996).

[33] M. Behr, D. Hastreiter, S. Mittal, and T. E. Tezduyar, ''Incompressible flow past a circular cylinder: dependence of the computed flow field on the location of the lateral boundaries,'' Comput. Methods Appl. Mech. Eng. **123**, 309 (1995).

[34] C. H. K. Williamson and A. Roshko. ''Vortex formation in the wake of an oscillating cylinder,'' J. Fluids Struct. **2**, 355 (1988).

[35] A. G. Tomboulides, G. S. Triantafyllou, and G. E. Karniadakis, ''A new mechanism of period doubling in free shear flows,'' Phys. Fluids A **4**, 1329 (1992).

[36] G. E. Karniadakis and G. S. Triantafyllou, ''Three-dimensional dynamics

and transition to turbulence in the wake of bluff objects,'' J. Fluid Mech. **238**, 1 (1992).
[37]M. Thompson, K. Hourigan, and J. Sheridan, ''Three-dimensional instabilities in the wake of a circular cylinder,'' Exp. Therm. Fluid Sci. **12**, 190 (1996).
[38]J. S. Bendat and A. G. Piersol, *Random Data—Analysis and Measurement Procedures*, 2nd ed. (Wiley, New York, 1986).
[39]C. Norberg, ''An experimental study of the circular cylinder in cross flow: transition around Re=5000,'' in *Proceedings of the 4th Asian Congress of Fluid Mechanics*, Hong Kong, August 1989, edited by N. W. M. Ko and S. C. Kot, University of Hong Kong, Suppl. Vol.
[40]M. Brede, H. Eckelmann, and D. Rockwell, ''On secondary vortices in the cylinder wake,'' Phys. Fluids **8**, 2117 (1996).
[41]A. Okajima and K. Sugitani, ''Strouhal number and base pressure coefficient of a rectangular cylinder,'' Trans. JSME Ser. B. **50**, 2004 (1984).
[42]C. Norberg (unpublished).
[43]B. R. Noack and H. Eckelmann, ''A global stability analysis of the steady and periodic cylinder wake,'' J. Fluid Mech. **270**, 297 (1994).
[44]S. Balachandar, R. Mittal, and F. M. Najjar, ''Properties of the mean recirculation region in the wakes of two-dimensional bluff bodies,'' J. Fluid Mech. **351**, 167 (1997).
[45]Y. Yokoi and K. Kamemoto, ''Initial stage of a three-dimensional vortex structure existing in a two-dimensional boundary layer separation flow (Observation of laminar boundary layer separation over a circular cylinder by flow visualization),'' JSME Int. J., Ser. III **35**, 189 (1992).
[46]Y. Yokoi and K. Kamemoto, ''Initial stage of a three-dimensional vortex structure existing in a two-dimensional boundary layer separation flow (Visual observation of laminar boundary layer separation over a circular cylinder from the side of a separated region),'' JSME. Int. J., Ser. B. **36**, 201 (1993).
[47]C. Norberg (unpublished).